Two voltage-dependent currents can explain the functional diversity of embryonic Renshaw cells

François Xavier Lejeune, Jean Marie Mangin, Juliette Boeri, Claude Meunier, Hervé Le Corronc, Pascal Branchereau, Yulia Timofeeva, François Xavier Lejeune, Christine Mouffle, Hervé Arulkandarajah, et al.

Two voltage-dependent currents can explain the functional diversity of embryonic Renshaw cells.

Juliette Boeri[1]¶, Claude Meunier[2]¶, Hervé Le Corronc[1,3]¶, Pascal Branchereau[4], Yulia Timofeeva[2,5,6], François Xavier Lejeune[7], Christine Mouffle[1], Hervé Arulkandarajah[1], Jean Marie Mangin[1], Pascal Legendre[1&]*, Antonny Czarnecki[1&]*

[1] INSERM, UMR_S 1130, CNRS, UMR 8246, Neuroscience Paris Seine, Institute of Biology Paris Seine, Sorbonne Univ, Paris, France.

[2] Centre de Neurosciences Intégratives et Cognition, CNRS UMR 8002, Institut Neurosciences et Cognition, Université de Paris, Paris, France.

[3] Univ Angers, Angers, France.

[4] Univ Bordeaux, INCIA, UMR 5287, Bordeaux, France.

[5] Department of Computer Science and Centre for Complexity Science, University of Warwick, Coventry, UK.

[6] Department of Clinical and Experimental Epilepsy, UCL Queen Square Institute of Neurology, University College London, London, UK.

[7] Institut du Cerveau et de la Moelle Epinière, Centre de Recherche CHU Pitié-Salpétrière, INSERM, U975, CNRS, UMR 7225, Sorbonne Univ, Paris, France.

* Corresponding authors
Email: pascal.legendre@inserm.fr (PL)
Email: antonny.czarnecki@sorbonne-universite.fr (AC)

¶These authors contributed equally to this work.

&These authors also contributed equally to this work.

Abstract

Spontaneous neuronal activity occurs at the onset of the synaptogenesis in the central Nervous System and plays a major role in shaping developing neural networks. How intrinsic properties of neurons evolve during this critical developmental period remains largely unknown. We studied the Renshaw cells because they participate to the early-synchronized neuronal activity in the embryonic spinal cord. We found that these interneurons are subdivided into several functional clusters at the onset of the synaptogenesis and then display a transitory involution process during which they lose their ability to sustain tonic firing. This complex developmental trajectory results from the synergy between a persistent sodium inward current and a delayed rectifier potassium outward current, which are present in most neurons during development and in the adult. Taken together, our results reveal a core mechanism producing functional hetereogeneity in embryonic neurons and likely shaping the ongoing of early spontaneous neuronal activity.

Keywords: development, spinal cord, embryo, Renshaw cell, firing pattern, functional involution, electrophysiology, biophysical modeling.

Introduction

The development of the central nervous system (CNS) follows complex steps, which depend on genetic and environmental factors and involve interactions between multiple elements of the neural tissue. Remarkably, emergent neurons begin to synchronize soon after the onset of synapse formation, generating long episodes of low frequency (<0.01 Hz) correlated spontaneous network activity (SNA) (Blankenship & Feller 2010, Hanson & Landmesser 2003, Khazipov & Luhmann 2006, Milner & Landmesser 1999, Momose-Sato & Sato 2013, Myers et al 2005, O'Donovan 1999, Saint-Amant 2010). In the mouse embryonic spinal cord (SC), SNA is driven by an excitatory cholinergic-GABAergic loop between motoneurons (MNs) and interneurons (INs), GABA being depolarizing before embryonic day 16.5 (E16.5) (Allain et al 2011). SNA emerges around E12.5 (Branchereau et al 2002, Czarnecki et al 2014, Hanson & Landmesser 2003, Myers et al 2005, Yvert et al 2004), at a time when functional neuromuscular junctions are not yet established (Pun et al 2002) and sensory and supraspinal inputs have not yet reached the spinal motor networks (Angelim et al 2018, Ballion et al 2002, Marmigere & Ernfors 2007, Ozaki & Snider 1997).

Several studies pointed out that SNA is an essential component in neuronal networks formation. (Hanson et al 2008, Katz & Shatz 1996, Moody & Bosma 2005, Spitzer 2006). In the SC, pharmacologically-induced disturbances of SNA between E12.5 and E14.5 induce defects in the formation of motor pools, in motor axon guidance to their target muscles and in the development of motor networks (Hanson & Landmesser 2004, Hanson & Landmesser 2006, Hanson et al 2008, Myers et al 2005). During SNA episodes, long lasting giant depolarization potentials (GDPs) are evoked in the SC, mainly by the massive release of GABA onto MNs (Czarnecki et al 2014). Renshaw cells ($V1^R$) are likely the first GABAergic partners of MNs in the mouse embryo (Benito-Gonzalez & Alvarez 2012, Boeri et al 2018),

and the massive release of GABA during SNA probably requires that many of them display repetitive action potential firing or plateau potential activity (Boeri et al 2018).

However, little is known about the maturation of the intrinsic properties and the firing pattern of embryonic $V1^R$. We recently found that $V1^R$ exhibit heterogeneous excitability properties when SNA emerges in the SC (Boeri et al 2018) in contrast to adult Renshaw cells that constitute a functionally homogeneous population (Bikoff et al 2016, Perry et al 2015). Whether this early functional diversity really reflects distinct functional classes of embryonic $V1^R$, how this diversity evolves during development, and what are the underlying biophysical mechanisms remain open questions. The impact of the functional diversity of $V1^R$ on MN activity during SNA episodes is also unknown. The present study addresses these issues using multiple approaches, including patch-clamp recordings, cluster analysis, biophysical modeling and dynamical systems theory. The firing patterns of $V1^R$ and the mechanisms underlying their functional diversity are analyzed during a developmental period covering the initial phase of development of SC activity in the mouse embryo (E11.5-E14.5), when SNA is present, and during the critical period (E14.5-E16.5), when GABAergic neurotransmission gradually shifts from excitation to inhibition and locomotor-like activity emerges (Branchereau et al 2002, Myers et al 2005, Yvert et al 2004).

We discover that the balance between the slowly inactivating subthreshold persistent sodium inward current (I_{Nap}) (Crill 1996) and the delayed rectifier potassium outward current (I_{Kdr}), accounts for the heterogeneity of embryonic $V1^R$ and the changes in firing pattern during development. The heterogeneity of $V1^R$ at E12.5 arises from the existence of distinct functional groups. Surprisingly, and in opposition to the classically accepted development scheme (Gao & Ziskind-Conhaim 1998, Gao & Lu 2008, Liu et al 2016, McKay & Turner 2005, Pineda & Ribera 2010, Sillar et al 1992), we show that the embryonic $V1^R$ population loses its ability to support tonic firing from E13.5 to E15.5, exhibiting a transient functional

involution during its development. Our experimental and theoretical results provide a global view of the developmental trajectories of embryonic $V1^R$. They demonstrate how a simple mechanism, based on the synergy of two major opposing voltage-dependent currents that are ubiquitous in neurons, can produce functional diversity.

Results

The delayed potassium rectifier current I_{Kdr} is a key partner of the persistent sodium current I_{Nap} in controlling embryonic $V1^R$ firing patterns during development

We previously highlighted that $V1^R$ are spontaneously active at E12.5. Their response to a 2 s suprathreshold depolarizing current steps revealed four main patterns, depending of the recorded interneuron (Boeri et al 2018): $V1^R$ firing only 1-3 APs at the onset depolarizing pulse, which were named single spiking (SS) $V1^R$, repetitive spiking (RS) $V1^R$ (Figure 1A), long-lasting sodium-dependent plateau potentials (PP) $V1^R$ and mixed events (ME) $V1^R$ that shows an alternation of action potentials (APs) and plateau potentials (Boeri et al 2018).

We also uncovered a relationship between I_{Nap} and the ability of embryonic $V1^R$ to sustain repetitive firing (Boeri et al 2018). However, the heterogeneous firing patterns of $V1^R$ observed at E12.5 could not be fully explained by variations in I_{Nap} (Boeri et al 2018) suggesting the involvement of other voltage-gated channels, in particular potassium channels, known to control firing and AP repolarization, play a role in controlling the firing pattern of $V1^R$. Our voltage clamp protocol did not reveal any inward rectifying current (hyperpolarizing voltage steps to -100 mV from V_H = -20 mV, data not shown), but we found two voltage-dependent outward potassium currents, a delayed rectifier current (I_{Kdr}) and a transient potassium current (I_A) in embryonic $V1^R$, whatever the firing pattern (Figures 1 B1, B2 and B3). These two currents are known to control AP duration and/or firing pattern (Coetzee et al 1999). The activation threshold of I_{Kdr} lied between -30 mV and -20 mV and the threshold of I_A between -60 mV and -50 mV, (n = 27) (Figures 1 C1, C2 and C3).

It was unlikely that the heterogeneity of $V1^R$ firing patterns resulted from variations in the intensity of I_A. Indeed its voltage-dependent inactivation (time constant: 23.3 ± 2.6 ms, n = 8), which occurs during the depolarizing phase of an AP, makes it ineffective to control AP or plateau potential durations. This was confirmed by our theoretical analysis (see Figure 10-

figure supplemental 1). We thus focused on I_{Kdr}. At E12.5, PP V1^R had a significantly lower G_{Kdr} (2.12 ± 0.44 nS, n = 6) than SS V1^R (5.57 ± 0.56 nS, n = 9) and RS V1^R (6.39 ± 0.83 nS, n = 7) (Figure 2A). In the same manner, PP V1^R at E12.5 had a significantly lower G_{Kdr} than SS V1^R at E14.5 (11.11 ± 1.12 nS, n = 10). However, there was no significant difference in G_{Kdr} between SS V1^R and RS V1^R at E12.5 (Figure 2A), which indicated that variations in G_{Kdr} alone could not explain all the firing patterns observed at E12.5. Similarly, there was no significant difference in G_{Nap} between RS V1^R (0.91 ± 0.08 nS, n = 8) and PP V1^R (1.24 ± 0.19 nS, n = 6) at E12.5 (Figure 2B), indicating that variations in G_{Nap} alone could not explain all the firing patterns of V1^R at E12.5 (Boeri et al 2018). In contrast G_{Nap} measured in SS V1^R at E12.5 (0.21 ± 0.06 nS, n = 9) were significantly lower compared to G_{Nap} measured in RS V1^R and in PP V1^R at E12.5 (Figure 2B).

Because the firing pattern of a neuron depends on the balance between outward currents and inward voltage-dependent currents (Coetzee et al 1999), we then hypothesized that the different firing patterns of V1^R observed at E12.5 were related to the G_{Nap} / G_{Kdr} ratio. We found that this ratio was significantly lower for SS V1^R recorded at E12.5 (G_{Nap} / G_{Kdr} = 0.043 ± 0.015, n = 9) or at E14.5 (0.012 ± 0.004, n = 10) compared to RS V1^R (0.154 ± 0.022, n = 8) and PP V1^R (0.66 ± 0.132, n = 6) recorded at the same age (Figure 2C). We also found that the G_{Nap} / G_{Kdr} ratio was significantly lower for RS V1^R compared to PP V1^R (Figure 2C).

Altogether, these results strongly suggest that, although the presence of I_{Nap} is required for embryonic V1^R to fire repetitively or to generate plateau potentials (Boeri et al 2018), the heterogeneity of the firing pattern observed between E12.5 is not determined by I_{Nap} *per se* but likely by a synergy between I_{Nap} and I_{Kdr}.

Manipulating the balance between G_{Nap} and G_{Kdr} changes embryonic V1^R firing patterns.

We previously showed that blocking I_{Nap} with riluzole converted PP V1^R or RS V1^R into SS V1^R (Boeri et al 2018). To confirm further that the balance between G_{Nap} and G_{Kdr} was the key factor in the heterogeneity of V1^R firing patterns, we assessed to what extent a given SS V1^R cell could change its firing pattern when I_{Kdr} was gradually blocked by 4-aminopiridine (4-AP). We found that I_{Kdr} could be blocked by μM concentrations of 4-AP (Figure 3) without affecting I_A (Figure 3-Figure supplement 1). 4-AP, applied at concentrations ranging from 0.3 μM to 300 μM, specifically inhibited I_{Kdr} (Figures 3 A1 and A2) with an IC_{50} of 2.9 μM (Figure 3B). These results favor the presence of the potassium channel subunit $K_{V3.1}$ (Gutman et al 2005, Liu & Kaczmarek 1998), which is known to be also present at postnatal stages in V1^R (Song et al 2006).

We then determined to what extent increasing the concentration of 4-AP modified the firing pattern of V1^R at E12.5. Applying 4-AP at concentrations ranging from 3 μM to 300 μM changed the firing pattern of SS V1^R recorded at E12.5 (n = 10) in a concentration-dependent manner (Figures 4 A1, A2 and A3). In 50% of the recorded V1^R, increasing 4-AP concentrations successfully transformed SS V1^R into PP V1^R with the following sequence: SS → RS → ME → PP (Figure 4A1). In a second group of embryonic V1^R (25%), 4-AP application only evoked mixed activity, with the same sequence as aforementioned (SS → RS → ME). In the remaining SS V1^R (25%), increasing 4-AP concentration only led to sustained AP firing (Figure 4A2). Application of 300 μM 4-AP on RS V1^R at E12.5 evoked mixed events or plateau potentials (Figure 4-figure supplement 1). Plateau potentials and repetitive spiking evoked in the presence of 300 μM 4-AP were fully blocked by 0.5-1 μM TTX, indicating that they were generated by voltage-gated Na^+ channels (Figures 4 B and C and Figure 4-figure supplement 1). It should be noted that the application of 300 μM of 4-AP induced a significant 30.5 ± 12.4 % increase (P = 0.0137; Wilcoxon test) of the input resistance (1.11 ± 0.08 GΩ versus 1.41 ± 0.12 GΩ; n = 11).

These results show that, in addition to I_{Nap}, the delayed rectifier potassium current is also a major determinant of the firing pattern of embryonic V1^R. They suggest that the firing pattern depends on a synergy between I_{Nap} and I_{Kdr} and that the different patterns can be ordered along the following sequence SS → RS → ME → PP when the ratio $G_{Nap}/\ G_{Kdr}$ is increased.

The heterogeneity of the* V1^R *firing patterns decreases during embryonic development

It was unclear whether these different firing patterns corresponded to well separated classes within the E12.5 V1^R population. To address this issue, we performed a hierarchical cluster analysis on 163 embryonic V1^R, based on three quantitative parameters describing the firing pattern evoked by the depolarizing pulse: the mean duration of evoked APs or plateau potentials measured at half-amplitude (mean ½Ad), the variability of the event duration during repetitive firing (coefficient of variation of ½Ad: CV ½Ad) and the total duration of all events, expressed in percentage of the pulse duration (depolarizing duration ratio: ddr) (Figure 5A inserts). In view of the large dispersion of mean ½Ad and ddr values, cluster analysis was performed using the (decimal) logarithm of these two quantities (Sigworth & Sine 1987). The analysis of the distribution of log mean ½Ad, CV ½Ad and log ddr revealed multimodal histograms that could be fitted with several Gaussians (Figure 5-Figure supplement 1 A1, B1 and C1). Cluster analysis based on these three parameters showed that the most likely number of clusters was 5 (Figures 5 A and B), as determined by the silhouette width measurement (Figure 5B). Two clearly separated embryonic V1^R groups with CV ½Ad = 0 stood out, as shown in the 3D plot in figure 5C. The cluster with the largest ½Ad (mean ½Ad = 833.5 ± 89.99 ms) and the largest ddr (0.441 ± 0.044) contained all PP V1^R (n = 35) (Figures 5C and D and Figure 5-Figure supplement 1 A2, B2 and C2). Similarly, the cluster with the shortest

205 ½Ad (9.73 ± 0.66 ms) and the lowest ddr (0.0051 ± 0.0004) contained all SS $V1^R$ (n = 46)
206 (Figures 5 C and D and Figure 5-Figure supplement 1 A2, B2 and C2).

207 The three other clusters corresponded to $V1^R$ with nonzero values of CV ½Ad (Figure 5C).
208 A first cluster regrouping all RS $V1^R$ (n = 69) was characterized by smaller values of ½Ad
209 (23.91 ± 1.43 ms), CV ½Ad (27.36 ± 1.64%) and ddr (0.11 ± 0.01) (Figures 5C and D and
210 figure 5-figure supplement 1 A2, B2 and C2). The last two clusters corresponded to ME $V1^R$
211 (Figures 1C and 1D). The smaller cluster, characterized by a larger CV ½Ad (170.9 ± 8.9%;
212 n= 4), displayed a mix of APs and short plateau potentials, while the second cluster, with
213 smaller CV ½Ad (87.61 ± 7.37%; n = 9), displayed a mix of APs and long-lasting plateau
214 potentials (Figure 5D and figure 5-figure supplement 1 B2). Their ½Ad and ddr values were
215 not significantly different (Figure 5-figure supplement 1 A2 and C2).

216 It must be noted that three embryonic $V1^R$ (1.8%) were apparently misclassified since they
217 were aggregated within the RS cluster although having zero CV ½Ad (Figure 5C; arrows).
218 Examination of their firing pattern revealed that this was because they generated only two
219 APs, although their ddr (0.16 to 0.2) and ½ Ad values (31.6 to 40.3 ms) were well in the range
220 corresponding of the RS cluster.

221 These different firing patterns of $V1^R$ might reflect different states of neuronal
222 development (Belleau & Warren 2000, Gao & Ziskind-Conhaim 1998, Picken Bahrey &
223 Moody 2003, Ramoa & McCormick 1994). Single spiking and/or plateau potentials are
224 generally believed to be the most immature forms of firing pattern, repetitive spiking
225 constituting the most mature form (Spitzer 2006, Tong & McDearmid 2012). If it were so, the
226 firing patterns of embryonic $V1^R$ would evolve during embryonic development from single
227 spiking or plateau potential to repetitive spiking, this latter firing pattern becoming the only
228 one in neonates (Perry et al 2015) and at early postnatal stages (Bikoff et al 2016). However,
229 RS neurons already represent 41% of $V1^R$ at E12.5. We therefore analyzed the development

of firing patterns from E11.5, when $V1^R$ terminate their migration and reach their final position (Alvarez et al 2013), to E16.5. This developmental period covers a first phase of development (E11.5-E14.5), where lumbar spinal networks exhibit SNA, and a second phase (E14.5-E16.5), where locomotor-like activity emerges (Allain et al 2010, Branchereau et al 2000, Myers et al 2005, Yvert et al 2004). We first analyzed changes in the intrinsic properties (input capacitance C_{in}, input resistance $R_{in} = 1/G_{in}$ and spike voltage threshold) of $V1^R$. C_{in} did not change significantly from E11.5 to E13.5 (Figure 6A), remaining of the order of 12 pF, in agreement with our previous work (Boeri et al 2018). However, it increased significantly at the transition between the two developmental periods (E13.5-E15.5) to reach about 23.5 pF at E15.5 (Figure 6A). A similar developmental pattern was observed for R_{in}, which remained stable during the first phase from E11.5 to E14.5 ($R_{in} \approx$ 1-1.2 GΩ) but decreased significantly after E14.5 to reach about 0.7 GΩ at E15.5 (Figure 2B). Spike threshold also decreased significantly between the first and the second developmental phases, dropping from about -34 mV at E12.5 to about -41 mV at E16.5 (Figure 2C). Interestingly, this developmental transition around E14.5 correspond to the critical stage at which SNA gives way to a locomotor-like activity (Allain et al 2010, Branchereau et al 2000, Yvert et al 2004) and rhythmic activity becomes dominated by glutamate release rather than acetylcholine release (Myers et al 2005).

This led us to hypothesize that this developmental transition could be also critical for the maturation of $V1^R$ firing patterns. The distinct firing patterns observed at E12.5 were already present at E11.5 (Figures 7 A and F), but the percentage of RS $V1^R$ strongly increased from E11.5 to E12.5, while the percentage of ME $V1^R$ decreased significantly (Figure 7F). The heterogeneity of $V1^R$ firing patterns then substantially diminished. Plateau potentials were no longer observed at E13.5, and ME $V1^R$ disappeared at E14.5 (Figures 7 C and F). Interestingly, the proportion of SS $V1^R$ remained high from E13.5 to E15.5 and even slightly

255 increased (91.23% at E14.5 and 93.33% at E15.5; Figure 7F). This trend was partially
256 reversed at E16.5, as the percentage of RS $V1^R$ increased at the expense of SS $V1^R$ (67.86 %
257 SS $V1^R$ and 32.34% RS $V1^R$; Figures 7 E and F). This decrease in repetitive firing capability
258 after E13.5 was surprising in view of what is classically admitted on the developmental
259 pattern of neuronal excitability (Moody & Bosma 2005, Spitzer et al 2000). Therefore, we
260 verified that it did not reflect the death of some $V1^R$ after E13.5. Our data did not reveal any
261 activated caspase3 (aCaspase3) staining in $V1^R$ (FoxD3 staining) at E14.5 (n = 10 SCs)
262 (Figure 8), in agreement with previous reports showing that developmental cell death of $V1^R$
263 does not occur before birth (Prasad et al 2008).

264 To determine to what extent the balance between G_{Nap} and G_{Kdr} was the key factor that
265 also determined the $V1^R$ firing patterns at E14.5 (Figures 7 C and F), we tested the effect of 4-
266 AP on single spiking $V1^R$ at this embryonic age. G_{Kdr}in SS $V1^R$ at E14.5 (11.11 ± 1.12 nS, n
267 = 10) was significantly high when compared to G_{Kdr} measured at E12.5 in SS $V1^R$ (Figure
268 2A). I_{NaP} can still be observed in $V1^R$ at E14.5 (Figure 9-Figure supplement 1). G_{Nap}
269 measured in SS $V1^R$ at E14.5 (0.13 ± 0.05 nS, n = 10) was similar to the G_{Nap}measured at
270 E12.5 in SS $V1^R$ (Figure 2B). At E14.5, 300 µM 4-AP inhibited only 59.2% of I_{Kdr}.
271 Increasing 4-AP concentration to 600 µM did not inhibit I_{Kdr} significantly more (60.2%)
272 (Figure 9-Figure supplement 2), indicating that inhibition of I_{Kdr} by 4-AP reached a plateau
273 at around 300 µM. 600 µM 4-AP application had no significant effect on I_A (Figure 9-Figure
274 supplement 2). The application of the maximal concentration of 4-AP tested (600 µM)
275 converted SS $V1^R$ (n = 13) to PP $V1^R$ (23.1%; Figures 9 A1 and B), RS $V1^R$ (38.5%; Figure 9
276 A2 and B) or ME $V1^R$ (38.4%; Figure 9B), as was observed at E12.5, thus indicating that the
277 firing pattern of $V1^R$ depends on the balance between I_{Nap} and I_{Kdr} also at E14.5. Plateau
278 potential and repetitive spiking recorded in the presence of 4-AP at E14.5 were fully blocked

by 0.5-1 μM TTX indicating that they were generated by voltage-gated Na^+ channels (Figures 9 A1 and A2), as observed at E12.5.

Theoretical analysis: basic model

As shown in Figure 10A for 26 cells, in which both G_{Nap} and G_{Kdr} were measured, the three largest clusters revealed by the hierarchical clustering analysis (SS, RS and PP, which account together for the discharge of more than 95% of cells, see Figure 5) correspond to well defined regions of the G_{Nap}- G_{Kdr} plane. Single spiking is observed only when G_{Nap} is smaller than 0.6 nS. For larger values of G_{Nap}, repetitive spiking occurs when G_{Kdr} is larger than 3.5 nS, and $V1^R$ display plateau potentials when G_{Kdr} is smaller than 3.5 nS. Mixed events (ME, 4.5% of the 163 cells used in the cluster analysis), where plateaus and spiking episodes alternate, are observed at the boundary of RS and PP clusters. This suggested to us that a conductance-based model incorporating only the leak current, I_{Nat}, I_{Nap} and I_{Kdr} (see Materials and Methods) could account for the experimental observations, the observed zonation being explained in terms of bifurcations between the different stable states of the model.

A one-parameter bifurcation diagram of the model is shown in Figure 10B for two values of G_{Kdr} (2.5 nS and 10 nS) and a constant injected current I = 20 pA. The slow inactivation of I_{Nap} was not taken into account at this stage of our analysis. For G_{Kdr} = 10 nS, the steady-state membrane voltage progressively increases (in gray) with G_{Nap}, but repetitive spiking (in red, see voltage trace for G_{Nap}= 1.5 nS) is not achieved until G_{Nap} reaches point SN_1, where a saddle node (SN) bifurcation of limit cycles occurs. This fits with the experimental data, where a minimal value of G_{Nap} is required for repetitive spiking (see also (Boeri et al 2018)), and is in agreement with the known role of I_{Nap} in promoting repetitive discharge (Kuo et al

2006, Taddese & Bean 2002). Below SN_1, the model responds to the onset of a current pulse by firing only one spike before returning to quiescence (see voltage trace for G_{Nap}= 0.1 nS), or a few spikes when close to SN_1 (not shown) before returning to quiescence. The quiescent state becomes unstable through a subcritical Hopf bifurcation (HB) at point HB_1, bistability between quiescence and spiking occurring between SN_1 to HB_1. Repetitive firing persists when G_{Nap} is increased further and eventually disappears at point SN_2. The firing rate does not change much throughout the RS range (Figure 10-Figure supplement 1 B), remaining between 11.9 Hz (at SN_1) and 17.1 Hz (at SN_2). A stable plateau appears at point HB_2 through a subcritical HB. The model is bistable between HB_2 and SN_2, plateau and large amplitude APs coexisting in this range.

The model behaves very differently when G_{Kdr} is reduced to 2.5 nS (gray-blue curve in Figure 10B). It exhibits a unique stable fixed point whatever the value of G_{Nap} is, and the transition from quiescence to plateau is gradual as G_{Nap} is increased. No repetitive spiking is ever observed. This indicates that the activity pattern is controlled not only by G_{Nap} but also by G_{Kdr}. This is demonstrated further in Figure 10C, where G_{Nap} was fixed at 1.5 nS while G_{Kdr} was increased from 0 to 25 nS. The model exhibits a plateau potential until G_{Kdr} is increased past point HB_2. Repetitive spiking then sets in, *via* a supercritical HB (in contrast to the subcritical bifurcation in Figure 10B for G_{Kdr} = 10 nS, see legend of Figure 10). The amplitude of AP decays to zero at HB_2, and no bistability occurs. When G_{Kdr} is further increased, repetitive firing eventually disappears through a SN bifurcation of limit cycles at point SN_1, the quiescent state becomes stable through a subcritical HB at point HB_1, and bistability occurs between these two points. This behavior is in agreement with Figure 10A.

Since both G_{Nap} and G_{Kdr} control the firing pattern of embryonic $V1^R$ cells, we computed a two-parameters bifurcation diagram (Figure 10D), where the different possible activity states and the transitions between them are plotted in the G_{Nap} - G_{Kdr} plane. The black lines

correspond to the bifurcations HB_1 and HB_2 and delimit a region where only repetitive firing occurs. The red lines correspond to the SN bifurcations of periodic orbits associated with the transition from quiescence to firing (SN_1) and the transition from plateau to firing (SN_2). They encompass a region (shaded area) where repetitive firing can be achieved but may coexist with quiescence (between the HB_1 and SN_1 lines) or plateau potential (in the narrow region between the HB_2 and SN_2 lines). We note that the SN_1 and SN_2 lines merge with the HB_1 and HB_2 lines at points B_1 and B_2, respectively. There, codimension-two Bautin bifurcations occur, and the bifurcations HB_1 and HB_2 switch from subcritical to supercritical case.

Some important features of the diagram must be emphasized: 1) minimal values of both G_{Nap} (to ensure sufficient excitability) and G_{Kdr} (to ensure proper spike repolarization) are required for repetitive spiking, 2) quiescence and plateau can be clearly distinguished only when they are separated by a region of repetitive spiking (see also Figure 10B for G_{Kdr}= 10 nS), otherwise the transition is gradual (Figure 9B for G_{Kdr}= 2.5 nS), 3) only oblique lines with an intermediate slope cross the bifurcation curve and enter the RS region (see, for example, the red line in Figure 10D). This means that repetitive spiking requires an appropriate balance between I_{Nap} and I_{Kdr}. If the ratio G_{Nap}/G_{Kdr} is too large (blue line) or too small (gray line), only plateau potentials or quiescence will be observed at steady state. This is exactly what is observed in experiments, as shown by the cumulative distribution function of the ratio G_{Nap}/G_{Kdr} for the different clusters of embryonic $V1^R$ in Figure 10E (same cells as in Figure 9A). The ratio increases according to the sequence SS → RS → ME → PP, with an overlap of the distributions for SS $V1^R$ and RS $V1^R$. Note also that the ratio for ME cells (around 0.25) matches the transition between repetitive spiking and plateau potentials in Figure 10D (more on this below).

Embryonic $V1^R$ cells display voltage fluctuations of up to 5 mV, presumably due to channel noise. The relatively low number of sodium and potassium channels (of the order of a

few thousands) led to voltage fluctuations in the stochastic version of our model comparable to those seen experimentally when the cell was quiescent (top voltage trace in Figure 10D) or when a voltage plateau occurred (bottom trace). Channel noise caused some jitter during repetitive spiking (middle trace), with some occasionally missing spikes (not shown), and induced clearly visible variations in the amplitude of APs. However, repetitive firing proved to be very robust and was not disrupted by voltage fluctuations. Altogether, channel noise little alters the dynamics (compare the deterministic voltage traces in Figure 10B and the noisy traces in Figure 10D). This is likely because channel noise has a broad power spectrum and displays no resonance with the deterministic solutions of the model.

The one-parameter bifurcation diagram of our model was not substantially modified when we took I_A into account, as shown in Figure 10-Figure supplement 1. It just elicited a slight membrane hyperpolarization, a rightward shift of the firing threshold and a decrease of the firing frequency. The transition from repetitive firing to plateau was not affected because I_A is inactivated by depolarization.

The bifurcation diagram of Figure 10D accounts qualitatively for the physiological data on $V1^R$ at E12.5 presented in Figure 10A, as shown in Figure 10E where the conductance data of Figure 10A were superimposed on it. Its exact position in the G_{Nap} - G_{Kdr} plane actually depends on the values of the passive parameters and it was computed in Figure 10D and F for G_{in}= 1 nS and C_{in}= 13 pF, the median values of the input capacitance and conductance at E12.5. Between E12.5 and E14.5, C_{in}, which provides an estimate of the cell size, increases by 38% in average, whereas G_{in} is not significantly modified (see Figure 6). As illustrated in Figure 9G the two-parameters bifurcation diagram is then shifted upward and rightward compared to Figure 10F, because larger conductances are required to obtain the same firing pattern. The observed regression of excitability from E12.5 to E14.5-E15.5 (see Figure 3) thus comes from a decrease in G_{Nap} density (see presumable developmental trajectories indicated

by arrow in Figure 10F) together with a shift of the RS region as cell size increases. As a result, all 9 cells shown in Figure 10G are deeply inside the SS region at E14.5.

It is a bit trickier to explain the experiments where 4-AP changed the firing pattern of SS $V1^R$ (Figure 4). This is because 4-AP decreases not only G_{Kdr} but also G_{in} and therefore the rheobase current. If we take these modifications of the input conductance and rheobase into account (Figure 10-Figure supplement 2), the bifurcation diagram remains qualitatively the same, but it is shifted toward the origin in the G_{Nap}- G_{Kdr} plane. The bifurcation lines between SS and RS (SN1) and between RS and PP (SN2) are then successively crossed when G_{Kdr} is reduced, in accordance with experimental results.

Theoretical analysis: extended model with slow inactivation of I_{Nap}

Our basic model accounts for the firing pattern of 73% of the 163 cells used in the cluster analysis. However, bursting, under the form of recurring plateaus separated by brief repolarization episodes (see a typical trace in Figure 11A left), was experimentally observed in half of PP $V1^R$ (24 out of 46) and plateaus intertwined with spiking episodes were recorded in the 13 cells of the ME cluster (8% of the total sample, see Figure 11A right for an example). Recurrent plateaus indicate membrane bistability. This requires that the $I-V$ curve be S-shaped, which occurs when anomalous rectification is large (large G_{Nap} and small G_{Kdr}, Figures 11B1 and 11B2). However, our basic model lacks a mechanism for switching between quiescent state and plateau. Channel noise might induce such transitions, but our numerical simulations showed that this is too infrequent to account for bursting (see voltage trace in Figure 11B1 where the plateau state is maintained despite channel noise).

To explain recurrent plateaus, we incorporated a slow dynamical process, namely the experimentally observed slow inactivation of I_{Nap}, in our model. The one-parameter bifurcation diagram of the basic model for G_{Kdr} = 2.5 nS is shown in Figure 11C. The

injected current was reduced from the value of 20 pA used in the previous section to 8 pA, so as to allow for bistability (Figure 10B2). The $G_{Nap} - V$ curve is then S-shaped, as shown in Figure 11B1, with a bistability region for G_{Nap} between 1.48 and 1.87 nS. This is in contrast with Figure 10B where the $G_{Nap} - V$ curve was monotonic. Adding the slow (de)inactivation of I_{Nap} caused periodic transitions between up (plateau) and down (quiescent) states, and the model then displayed a stable limit cycle (shown in black in Figure 11C), as illustrated by the top voltage trace on the right. This mechanism is known as pseudo-plateau or plateau-like bursting (a.k.a. fold-subcritical HB bursting) (Teka et al 2011). It is akin to square wave bursting (Bertram et al 1995, Borisyuk & Rinzel 2005, Izhikevich 2000a, Rinzel 1985), but the up-state is a stable fixed point rather than a limit cycle (Osinga et al 2012, Osinga & Tsaneva-Atanasova 2010, Stern et al 2008), which is why recurrent plateaus are obtained rather than bursts of APs. The duration of the plateaus and repolarization episodes depends on the values of G_{Nap}, G_{Kdr} and I, but it is also largely controlled by the inactivation kinetics. A voltage-independent time constant τ_s leads to up and down states of comparable durations (see top voltage trace in Figure 11C), the duration of which increases with τ_s. Making τ_s voltage-dependent changes the relative durations of plateaus and repolarization episodes. If τ_s decreases with membrane voltage, for instance, repolarization episodes are shortened (bottom voltage trace). Adding channel noise preserves bursting but introduces substantial randomness in the duration of plateaus and repolarization episodes (middle voltage trace). We also noted that adding the I_A current lengthened the repolarizing phase (Figure 10-Figure supplement 1).

Slow inactivation of $\boldsymbol{I_{Nap}}$ also provides an explanation for mixed patterns, where plateaus alternate with spiking episodes (Figure 11A, right). They take place in our model near the transition between repetitive spiking and plateau, as in experiments (Figure 10A). Slow

inactivation (V_s = -30 mV, k_s = -5 mV) can lead to elliptic bursting (Izhikevich 2000b, Su et al 2004) when the bifurcation HB_2 is subcritical and located near the Bautin bifurcation B_2, which is the case here (Figure 10D). The model then displays a stable limit cycle with alternating plateaus and spiking episodes, arising from crossing the bifurcation points HB_2 and SN_2 back and forth (see bifurcation diagram in Figure 11D and top voltage trace). We note that sufficient deinactivation of I_{Nap} for triggering a new plateau is difficult to be achieved during spiking episodes, because voltage oscillates over a large range and variations of the inactivation level are largely averaged out. Therefore, we had to choose a shallower inactivation curve than for pseudo-plateau bursting together with a more depolarized half-inactivation voltage to achieve elliptic bursting. Otherwise, the model keeps on spiking repetitively without returning to the plateau state. This is probably why it is difficult in many recorded cells to elicit plateaus by increasing the injected current, an experimental observation that was not explained by our basic model.

When τ_s is voltage-dependent and small enough in the subthreshold voltage range, there is not enough time for APs to be fired between plateaus (see bottom voltage trace in Figure 11D). One then observes successive plateaus with superimposed voltage oscillations that decay at plateau onset and grow at offset. Both types of plateaus, with voltage oscillations (elliptic bursting) and without (pseudo-plateau bursting) were observed in the embryonic $V1^R$ we recorded. Finally, we note that bistability between plateau and repetitive spiking is not necessary for elliptic bursting, which may also be due to the slow passage through HB_2 when this Hopf bifurcation is supercritical (Baer et al 1989, Holden & Erneux 1993). Slow inactivation of I_{Nap} then leads to a delayed destabilization of the plateau after HB_2 is crossed, while deinactivation during repetitive spiking leads to the crossing of HB_2 in the opposite direction and a delayed restabilization of the plateau (not shown).

Altogether, our study shows that a model incorporating the slow inactivation of I_{Nap} accounts for all the firing patterns displayed by cells of the PP and ME clusters.

4-AP increased GABAergic inputs on MNs at E12.5

During SNA, MNs receive massive inputs from GABAergic INs and, to a lesser extent, from glutamatergic INs. This leads to the occurrence of Giant Depolarizing Potential (GDPs) (Czarnecki et al 2014). $V1^R$ are likely the first INs to release GABA at E12.5 (Boeri et al 2018). However, it is unclear how the heterogeneity of the activity patterns observed in $V1^R$ shapes GABA-evoked current in MNs, even though I_{Nap} appears essential for the occurrence of GDPs and SNA in the SC at E12.5 (Boeri et al 2018). To address this issue, we took advantage of the ability of 4-AP to change the activity pattern of $V1^R$. We focused our analysis on the evoked GABAergic Giant Inward Currents (GICs) (voltage clamp recordings; E_{Cl} = -30 mV) and GABAergic GDPs (current clamp recordings). GICs and GDPs were induced by a 1 ms stimulation applied at the cervical level of the SC while recording lumbar MNs (Figure 12A) in the presence of the broad-spectrum glutamate receptor antagonist kynurenic acid (4 mM). At E12.5, 4-AP increased the amplitude of GABAergic GICs (155 ± 86 pA vs 191 ± 112 at 30 μM, and 206 ± 115 pA at 300 μM, n = 6) and the GICs half-width (0.57 ± 0.28 s vs 1.01 ± 0.34 s at 30 μM, and 1.32 ± 0.34 s at 300 μM, n = 6) (Figures 12 B1 and B2). When analyzing GDPs, we observed a strong increase of their half-width in the presence of 4-AP (1.9 ± 0.4 s vs 3.8 ± 1.3 s at 30 μM, and 3.6 ± 1.1 s at 300 μM, n = 8) but no significant change in their amplitude (30.5 ± 7.2 mV vs 32.6 ± 6.4 mV at 30 μM and 33.4 ± 7.2 mV at 300 μM, n = 8), nor in the firing rate of MNs (Figures 12 C1 and C2). Increasing the proportion of GABAergic INs that sustain repetitive firing or plateau potential activity likely enhances the release of GABA on MNs as exemplified by the increased evoked GABAergic current on MNs. However, the lack of effects on GDP amplitude and on MN

476 firing indicates that the biophysical properties of MNs buffer variations in the intensity of
477 their GABAergic inputs. This is likely due to a combination of the depolarized equilibrium
478 potential of chloride at this embryonic age (ECl = -30 mV; (Allain et al 2011)) and the
479 relatively high input resistance of E12.5 MNs (0.3-1 GΩ) (Czarnecki et al 2014)), allowing
480 relatively small changes in GABAergic conductance to evoke a voltage response with
481 maximum amplitude. Such a process probably contributes to the robustness of MN activity
482 during episodes of SNA.

Discussion

$V1^R$ constitute a homogeneous population in terms of their transcription factor program during development (Benito-Gonzalez & Alvarez 2012, Stam et al 2012), their physiological function (Eccles et al 1956) and their firing pattern at postnatal stages (Bikoff et al 2016). Surprisingly, our electrophysiological recordings and our cluster analysis clearly indicate that distinct functional classes of $V1^R$ are transiently present during development at the onset of the SNA (E11.5-E12.5). Five different groups of embryonic $V1^R$ were defined using cluster analysis, according to their firing properties.

Development of the firing pattern of embryonic $V1^R$ during SNA

It is generally assumed that, during early development, newborn neurons cannot sustain repetitive firing (Pineda & Ribera 2010, Spitzer et al 2000). Later on, neurons progressively acquire the ability to fire repetitively, APs become sharper, and neurons eventually reach their mature firing pattern, due to the progressive appearance of a panoply of voltage-gated channels with different kinetics (Moody & Bosma 2005, Pineda & Ribera 2010, Spitzer et al 2000). Our results challenge the general view that single spiking is a more immature form of excitability (Pineda & Ribera 2010). Indeed, we show that repetitive firing and plateau potentials dominated at early stages (E11.5-E12.5), single spiking prevailing only later (E13.5- E16.5).

The different $V1^R$ firing patterns observed at E11.5-E12.5 might reflect variability in the maturation level between $V1^R$ at a given developmental stage, as suggested for developing MNs (Durand et al 2015, Vinay et al 2000). However, this is unlikely since $V1^R$ transiently lose their ability to sustain tonic firing or plateau potential after E13.5. The heterogeneous discharge patterns of $V1^R$ observed before E13.5 contrasts with the unique firing pattern of $V1^R$ at postnatal age (Bikoff et al 2016). Accordingly, the transient functional heterogeneity

of $V1^R$ rather reflects an early initial developmental stage (E11.5-E13.5) of intrinsic excitability.

The physiological meaning of the transient functional involution of $V1^R$ that follows, after E12.5, is puzzling. To our knowledge, such a phenomenon was never described in vertebrates during CNS development. So far, a functional involution was described only for inner hair cells between E16 and P12 (Marcotti et al 2003a, Marcotti et al 2003b) and cultured oligodendrocytes (Sontheimer et al 1989), and it was irreversible. Because most $V1^R$ cannot sustain tonic firing after E12.5, it is likely that their participation to SNA is limited to the developmental period before other GABAergic interneuron subtypes mature and start to produce GABA and glycine (Allain et al 2004). Interestingly, embryonic $V1^R$ begin to recover their capability to sustain tonic firing when locomotor-like activity emerges (Myers et al 2005, Yvert et al 2004), a few days before they form their recurrent synaptic loop with MNs (around E18.5 in the mouse embryos, (Sapir et al 2004)). One possible function of the transient involution between E12.5 and E15.5 could be to regulate the growth of $V1^R$ axons toward their targets. It is indeed known that low calcium fluctuations within growth cones are required for axon growth while high calcium fluctuations stop axon growth and promote growth cone differentiation (Henley & Poo 2004).

Ion channels mechanisms underlying the functional heterogeneity of embryonic $V1^R$

Blockade of I_{Nap} leads to single spiking (Boeri et al 2018), which emphasizes the importance of this current for the occurrence of repetitive firing and plateau potentials in $V1^R$ at early development stages. But these neurons can also switch from one firing pattern to another, when G_{Kdr} is decreased by 4-AP, which emphasizes the importance of I_{Kdr}. We found that the main determinant of embryonic $V1^R$ firing pattern is the balance between G_{Nap} and G_{Kdr}.

A Hodgkin-Huxley-like model incorporating a persistent sodium current I_{Nap} provided a parsimonious explanation of all the firing patterns recorded in the $V1^R$ population at E12.5, even in details. It provided a mathematical interpretation for the clustering of embryonic $V1^R$ shown by the hierarchical analysis and accounted for the effect of 4-AP and riluzole (Boeri et al 2018) on the discharge. Remarkably, it highlights how a simple mechanism involving only the two opposing currents I_{Nap} and I_{Kdr} can produce functional diversity in a population of developing neurons. The model explains why minimal G_{Nap} and G_{Kdr} are required for firing, how a synergy between G_{Nap} and G_{Kdr} controls the firing pattern, and it accounts for the zonation of the $G_{Nap} - G_{Kdr}$ plane that is observed experimentally.

Adding the slow inactivation of I_{Nap} to the model allowed us to account for the bursting patterns displayed by cells of the PP and ME clusters. We showed, in particular, that mixed events arose from elliptic bursting at the repetitive spiking-plateau transition and that smooth repetitive plateaus could be explained by a pseudo-plateau bursting mechanism (Osinga & Tsaneva-Atanasova 2010, Teka et al 2011). Such bursting scenario has been previously studied in models of endocrine cells (Stern et al 2008, Tagliavini et al 2016, Tsaneva-Atanasova et al 2010) and adult neurons (Oster et al 2015), but rarely observed in experiments.

Heterogeneity of the discharge pattern of pacemaker neurons has also been observed in the embryonic pre-Bötzinger network (Chevalier et al 2016). However, it is related there to the gradual change of balance between two inward currents, I_{Nap} and the calcium-activated nonselective cationic current I_{CAN}, during neuronal maturation, which leads to the progressive replacement of pseudo-plateau bursting by elliptic bursting. Such a scenario cannot account for the variety of discharge patterns observed in embryonic $V1^R$ at the E11.5-12.5 stage of development (Boeri et al 2018). Our theoretical analysis and our experimental data clearly indicate that competition and synergy between two opposing currents are necessary to explain all the firing patterns of $V1^R$. We also note that our model is not restricted to embryonic $V1^R$,

but may also apply to any electrically compact cell, the firing activity of which is dominated by sodium and delayed rectifier potassium currents. This is the case of many classes of embryonic cells in mammals at an early stage of their development.

Altogether our experimental and theoretical results provide a global view of the developmental trajectories of embryonic $V1^R$ (see Figures 9F and 9G). At E12.5, conductances of embryonic $V1^R$ are widely spread in the $G_{Nap} - G_{Kdr}$ plane, which explains the heterogeneity of their firing patterns. This likely results from the random and uncorrelated expression of sodium and potassium channels from cell to cell at this early stage. Between E12.5 and E14.5-15.5 cell size increases, and G_{Kdr} with it, while the density of sodium channels decreases (see Figures 6 and 9). The functional involution displayed by $V1^R$ between E12.5 and E15.5 thus mainly results from a decrease of G_{Nap} coordinated with an increase of G_{Kdr}. How these synergistic processes are controlled during this developmental period remains an open issue.

Physiological implications of the G_{Nap} - G_{Kdr} synergy in $V1^R$ at the onset of the SNA

The increase in GABA-ergic GIC amplitude and duration in the presence of 4-AP suggests that 4-AP, by changing the G_{Nap} /G_{Kdr} ratio and the input conductance increases embryonic $V1^R$ excitability, which in turn augments GABA release onto MNs. This fits with the view according to which repetitive firing is more efficient than single spiking at evoking calcium entry and promoting vesicular release at presynaptic terminals, plateau potentials being even more efficient (Hallermann & Silver 2013, Tibbs et al 1989, Wang & Kaczmarek 1998). It must however be noted that although 4-AP increased GDP duration, this potassium blocker had little effect on GDP amplitude and on MN firing, indicating that MN activity is poorly affected by variations in GABA release. This can be explained by the depolarized equilibrium potential of chloride ions at this developmental age (-30 mV) (Delpy et al 2008) and by the

583 high input resistance of MNs, which limits the number of activated $GABA_A$ receptors needed
584 for generating a GDP of maximal amplitude. In addition, most MNs are not able to sustain
585 tonic firing during a GDP at E12.5 (Czarnecki et al 2014), which prevents increase in GDP
586 duration from increasing MN firing rate.

587 Due to their functional involution $V1^R$ must become less efficient to generate GABAergic
588 GICs on MNs after E12.5. However, this is unlikely to impact SNA on MNs since $V1^R$ loose
589 their ability to sustain tonic firing at a time when other interneurons begin to produce GABA
590 (Allain et al 2011). We cannot completely rule out that some other INs than $V1^R$ were also
591 affected by 4-AP application already at E12.5, but it is important to note that $V1^R$ are the first
592 INs contacting MNs and producing GABA at this age in the embryonic SC (Boeri et al 2018),
593 which makes them the best candidates to explain the effect of 4-AP.

594 Our model is not restricted to embryonic $V1^R$. It may also apply to any electrically
595 compact cell or to the axon initial segment where G_{Nap} and G_{Kdr} play a major role in the
596 occurrence of repetitive firing (Kole & Stuart 2012). It is noteworthy that, even though the
597 nature of the firing pattern is determined only by the synergy of G_{Nap} and G_{Kdr} in our model,
598 its quantitative features also depend on the input conductance. This implies that changes in
599 G_{input} evoked by local synaptic activity may alter the firing pattern of the postsynaptic neurons.
600 Interestingly, the initial segment of cortical and hippocampal pyramidal neurons receive
601 GABAergic inputs (Kole & Stuart 2012).

602

603 ***Conclusions***

604 In conclusion, our results indicate for the first time that a single mechanism involving two
605 classes of ubiquitous voltage-gated channels with opposite functions that are ubiquitous in
606 neurons is sufficient to produce functional diversity between neurons. It accounts for the

607 unusual developmental pattern of immature $V1^R$ during the important time window where

608 SNA is expressed in the embryonic spinal cord.

609

610 ## Materials and Methods

611 ***Isolated spinal cord preparation.***

612 Experiments were performed in accordance with European Community guiding principles
613 on the care and use of animals (86/609/CEE, CE Off J no. L358, 18 December 1986), French
614 decree no. 97/748 of October 19, 1987 (J Off République Française, 20 October 1987, pp.
615 12245-12248). All procedures were carried out in accordance with the local ethics committee
616 of local Universities and recommendations from the CNRS. We used GAD67eGFP knock-in
617 mice to visualize putative GABAergic INs (Tamamaki et al 2003), as in our previous study
618 (Boeri et al 2018). To obtain E12.5-E16.5 transgenic GAD67-eGFP embryos, 8 to 12 weeks
619 old wild-type Swiss female mice were crossed with GAD67-eGFP Swiss male mice.

620 Isolated mouse SCs from 420 embryos were used in this work and obtained as previously
621 described (Delpy et al 2008, Scain et al 2010). Briefly, pregnant mice were anesthetized by
622 intramuscular injection of a mix of ketamine and xylazine and sacrificed using a lethal dose of
623 CO_2 after embryos of either sex were removed. Whole SCs were isolated from eGFP-positive
624 embryos and maintained in an artificial cerebrospinal fluid (ACSF) containing 135 mM NaCl,
625 25 mM $NaHCO_3$, 1 mM NaH_2PO_4, 3 mM KCl, 11 mM glucose, 2 mM $CaCl_2$, and 1 mM
626 $MgCl_2$ (307 mOsm/kg H_2O), continuously bubbled with a 95% O_2-5% CO_2 gas mixture.

627 In the lumbar SC of GAD67eGFP mouse embryos, eGFP neurons were detected using 488
628 nm UV light. They were localized in the ventro-lateral marginal zone between the motor
629 columns and the ventral funiculi (Stam et al 2012). Embryonic $V1^R$ identity was confirmed by
630 the expression of the forkhead transcription factor Foxd3 (Boeri et al 2018).

631

632 ***Whole-cell recordings and analysis***

633 The isolated SC was placed in a recording chamber and was continuously perfused (2

ml/min) at room temperature (22-26°C) with oxygenated ACSF. Whole-cell patch-clamp recordings of lumbar spinal embryonic $V1^R$ were carried out under direct visualization using an infrared-sensitive CCD video camera. Whole-cell patch-clamp electrodes with a resistance of 4-7 MΩ were pulled from thick-wall borosilicate glass using a P-97 horizontal puller (Sutter Instrument Co., USA). They were filled with a solution containing (in mM): 96.4 K methanesulfonate, 33.6 KCl, 4 $MgCl_2$, 4 Na_2ATP, 0.3 Na_3GTP, 10 EGTA, and 10 HEPES (pH 7.2; 290 mOsm/kg-H_2O). This intracellular solution led to an equilibrium potential of chloride ions, E_{Cl}, of about -30 mV, close to the physiological values measured at E12.5 in spinal MNs (Delpy et al 2008). The junction potential (6.6 mV) was systematically corrected offline.

Signals were recorded using Multiclamp 700B amplifiers (Molecular Devices, USA). Data were low-pass filtered (2 kHz), digitized (20 kHz) online using Digidata 1440A or 1550B interfaces and acquired using pCLAMP 10.5 software (Molecular Devices, USA). Analyses were performed off-line using pCLAMP 10.5 and Axograph 1.7.2 (Molecular devices; RRID:SCR_014284) software packages.

In voltage-clamp mode, voltage-dependent K^+ currents (I_{Kv}) were elicited by 500 ms depolarizing voltage steps (10 mV increments, 10 s interval) after a prepulse of 300 ms at V_H = -100 mV. To isolate I_{Kdr}, voltage steps were applied after a 300 ms prepulse at V_H = -30 mV that inactivated the low threshold transient potassium current I_A. I_A was then obtained by subtracting offline I_{Kdr} from the total potassium current I_{Kv}. Capacitance and leak current were subtracted using on-line P/4 protocol provided by pCLAMP 10.5.

In current-clamp mode, $V1^R$ discharge was elicited using 2 s depolarizing current steps (from 0 to ≈ 50 pA in 5-10 pA increments, depending on the input resistance of the cell) with an 8 s interval to ensure that the membrane potential returned to V_H. When a cell generated a

sustained discharge, the intensity of the depolarizing pulse was reduced to the minimal value compatible with repetitive firing.

I_{Nap} was measured in voltage-clamp mode using a 70 mV/s depolarizing voltage ramp (Huang & Trussell 2008). This speed was slow enough to preclude substantial contamination by the inactivating transient current and fast enough to avoid substantial inactivation of I_{Nap}. Subtraction of the current evoked by the voltage ramp in the presence of 1 µM tetrodotoxin (TTX) from the control voltage ramp-evoked current revealed I_{Nap}.

Pharmacological reagents

During patch-clamp recordings, bath application of TTX (1 µM, Alomone, Israel) or 4-AP (0.3 - 600 µM, Sigma) was done using 0.5 mm diameter quartz tubing positioned, under direct visual control, 50 µm away from the recording area. The quartz tubing was connected to 6 solenoid valves linked with 6 reservoirs *via* a manifold. Solutions were gravity-fed into the quartz tubing. Their application was controlled using a VC-8 valve controller (Warner Instruments, USA).

4-aminopyridine (4-AP; Sigma Aldrich, USA) was used to block I_{Kdr}. To determine the concentration–response curve, $I-V$ curves of I_{Kdr} for different concentrations of 4-AP (0.3 to 300 µM) were compared to the control curve obtained in the absence of 4-AP. The percentage of inhibition for a given concentration was calculated by dividing the peak intensity of I_{Kdr} by the peak value obtained in control condition. The obtained normalized concentration–response curves were fitted using the Hill equation:

$$\frac{100-I_{min}}{1+([4-AP]/IC_{50})^{n_H}}+I_{min}\ ,$$

where [4-AP] is the 4-AP concentration, I_{min} is the residual current (in percentage of the peak I_{Kdr}), $100-I_{min}$ is the maximal inhibition achieved for saturating concentration of 4-AP,

682 IC_{50} is the 4-AP concentration producing half of the maximal inhibition, and n_H is the Hill
683 coefficient. Curve fitting was performed using KaleidaGraph 4.5 (Synergy Software, USA).
684
685 ***Immunohistochemistry and confocal microscopy***
686 E14.5 embryos were collected from pregnant females. Once dissected out of their yolk sac,
687 SCs were dissected and immediately immersion-fixed in phosphate buffer (PB 0.1 M)
688 containing 4% paraformaldehyde (PFA; freshly prepared in PB, pH 7.4) for 1 h at 4°C. Whole
689 SCs were then rinsed out in 0.12 M PB at 4°C, thawed at room temperature, washed in PBS,
690 incubated in NH_4Cl (50 mM), diluted in PBS for 20 min and then permeabilized for 30 min in
691 a blocking solution (10% goat serum in PBS) with 0.2% Triton X-100. They were incubated
692 for 48 h at 4°C in the presence of the following primary antibodies: guinea pig anti-FoxD3
693 (1:5000, gift from Carmen Birchmeier and Thomas Müller of the Max Delbrück Center for
694 Molecular Medicine in Berlin) and rabbit anti-cleaved Caspase-3 (1:1000, Cell Signaling
695 Technology Cat# 9661, RRID:AB_2341188). SCs were then washed in PBS and incubated
696 for 2 h at RT with secondary fluorescent antibodies (goat anti-rabbit-conjugated 649; donkey
697 anti-guinea pig-conjugated Alexa Fluor 405 [1:1000, ThermoFisher]) diluted in 0.2% Triton
698 X-100 blocking solution. After washing in PBS, SCs were dried and mounted in Mowiol
699 medium (Millipore, Molsheim, France). Preparations were then imaged using a Leica SP5
700 confocal microscope. Immunostaining was observed using a 40X oil-immersion objective
701 with a numerical aperture of 1.25, as well as with a 63X oil-immersion objective with a
702 numerical aperture of 1.32. Serial optical sections were obtained with a Z-step of 1 µm (40X)
703 and 0.2-0.3 µm (63X). Images (1024x1024; 12-bit color scale) were stored using Leica
704 software LAS-AF and analyzed using ImageJ 1.5 (N.I.H., USA; http//rsb.info.nih.gov/ij/) and
705 Adobe Photoshop CS6 (Adobe, USA) software.
706

Cluster analysis

To classify the firing patterns of embryonic $V1^R$, we performed a hierarchical cluster analysis on a population of 163 cells. Each cell was characterized by three quantitative measures of its firing pattern (see legend of Fig 1). After normalizing these quantities to zero mean and unit variance, we performed a hierarchical cluster analysis using the hclust function in R software (version 3.3.2, https://cran.r-project.org/) that implements the complete linkage method. The intercluster distance was defined as the maximum Euclidean distance between the points of two clusters, and, at each step of the process, the two closest clusters were merged into a single one, thus constructing progressively a dendrogram. Clusters were then displayed in data space using the dendromat function in the R package 'squash' dedicated to color-based visualization of multivariate data. The best clustering was determined using the silhouette measure of clustering consistency (Rousseeuw 1987). The silhouette of a data point, based on the comparison of its distance to other points in the same cluster and to points in the closest cluster, ranges from -1 to 1. A value near 1 indicates that the point is well assigned to its cluster, a value near 0 indicates that it is close to the decision boundary between two neighboring clusters, and negative values may indicate incorrect assignment to the cluster. This allowed us to identify an optimal number k of clusters by maximizing the overall average silhouette over a range of possible values for k (Rousseeuw 1987), using the silhouette function in the R package 'cluster'.

Biophysical modeling

To understand the relationship between the voltage-dependent membrane conductances and the firing patterns of embryonic $V1^R$, we relied on a single compartment conductance based model that included the leak current, the transient and persistent components of the

sodium current, I_{Nat} and I_{Nap}, and a delayed rectifier potassium current I_{Kdr}. Voltage evolution then followed the equation

$$C_{in}\frac{dV}{dt} = G_{in}(V_H - V) + G_{Nat}m^3h(E_{Na} - V) + G_{Nap}m_p^3(E_{Na} - V) + G_{Kdr}n^3(E_K - V) + I \quad (1),$$

where C_{in} was the input capacitance; G_{in} the input conductance; G_{Nat}, G_{Nap}, G_{Kdr} the maximal conductances of the aforementioned currents; m, m_p and n their activation variables; h the inactivation variable of I_{Nat}; V_H the baseline potential imposed by *ad hoc* current injection in current-clamp experiments; E_{Na} and E_K the Nernst potentials of sodium and potassium ions, and I the injected current. All gating variables satisfied equations of the form:

$$\tau_x\frac{dx}{dt} = x_\infty(V) - x,$$

where the (in)activation curves were sigmoid functions of the form:

$$x_\infty = \frac{1}{1+\exp\left(-(V-V_x)/k_x\right)}$$

with k_x being positive for activation and negative for inactivation. The time constant τ_x was voltage-independent except for the inactivation variable h.

To take into account the inactivating potassium current I_A revealed by experiments, we also considered a model with the additional term $G_Am_Ah_A(E_K - V)$ added to the right-hand-side of equation (1). The activation variable m_A of I_A was assumed to follow any voltage change instantaneously while its inactivation variable evolved more slowly.

To explain the more complex activity patterns observed in 27 % of the cells, we added a slow inactivation variable s to I_{Nap}, which became $G_{Nap}m_p^3s(V_{Na} - V)$. We considered that the corresponding time constant τ_s could be voltage-dependent.

The effect of channel noise was investigated with a stochastic realization of the model, where channels kinetics were described by Markov-type models, assuming a unitary channel conductance of 10 pS for all channels.

754 Most model parameters were chosen on the basis of experimental measurements (see S1
755 File). Parameters that could not be constrained from our experimental data were chosen from
756 an experimentally realistic range of values.
757
758 ***Choice of model parameters***
759 V_H was set to -60 mV. C_{in} (average 13.15 pF, 50% between 11.9 and 15.1 pF, only 18
760 cells out of 246 in the first quartile below 7.2 pF or in the fourth quartile above 19 pF) and
761 G_{in} (50% of cells between 0.71 and 1.18 nS, only 7 out of 242 with input conductance above
762 2 nS) were not spread much in the cells recorded at E12.5, showing that most embryonic $V1^R$
763 were of comparable size. Interestingly, C_{in} and G_{in} were not correlated, which indicated that
764 the input conductance was determined by the density of leak channels rather than by the sheer
765 size of the cell. Moreover, no correlation was observed between the passive properties and the
766 firing pattern (Boeri et al 2018). Therefore, we always set G_{in} and C_{in} to 1 nS and 13 pF in
767 the model (except in Figure 10-Figure supplement 2), close to the experimental medians (0.96
768 nS and 13.15 pF, respectively). The membrane time constant C_{in}/G_{in} was then equal to 13
769 ms, which was also close to the experimental median (13.9 ms, N=241).
770 E_{Na} was set to a standard value of 50 mV. The activation curve of I_{Nap} was obtained by
771 fitting experimental data, leading to a mid-activation of -33 mV and a steepness of 11 mV.
772 The experimentally measured values of G_{Nap} were in the range 0-2.2 nS. We assumed that the
773 activation curve of I_{Nat} was shifted rightward by 6 mV in comparison to I_{Nap}. No
774 experimental data was available for the inactivation of I_{Nat}. We chose a mid-inactivation
775 voltage V_h= -45 mV and a steepness k_h=-5 mV. We also assumed that the activation time
776 constant of both I_{Nat} and I_{Nap} was 1.5 ms, and that the inactivation time constant was
777 voltage-dependent: $\tau_h(V) = 16.5 - 13.5\tanh((V+20)/15)$, decreasing by one order of
778 magnitude (from 30 ms down to 3 ms) with the voltage increase. This enabled us to account

779 for the shape of the action potentials recorded in experiments, showing a slow rise time and
780 rather long duration. The conductance G_{Nat} was not measured experimentally. When
781 choosing a reasonable value of 25 nS for G_{Nat}, the model behaved very much as recorded
782 embryonic V1^{R}: similar current threshold (typically 10-20 pA) and stable plateau potential
783 obtained for the largest values of G_{Nap}.

784 When investigating how repetitive plateaus were generated (see Fig 10C), we chose V_s = -
785 30 mV for the mid-inactivation of I_{Nap} and set the steepness k_s at -5 mV (as for the
786 inactivation of I_{Nat}). To account for mixed events (and oscillatory plateaus, see Fig 10D), we
787 had to shift the inactivation curve (V_s = -20 mV) and make it less steep (k_s = -15 mV), so as
788 to ensure sufficient de-inactivation of I_{Nap} during spiking episodes.

789 E_K was set to a standard value of -80 mV. The activation parameters of I_{Kdr} were obtained
790 by fitting the experimental data: V_n = -20 mV, k_n = 20 mV, τ_n = 10 ms and an activation
791 exponent of 3. The activation and inactivation properties of I_A were also chosen based on
792 experimental measurements. Accordingly, V_{m_A} = -30 mV, k_{m_A} = -12 mV, V_{h_A} = -70 mV,
793 k_{h_A} = -7 mV, and τ_{h_A}= 23 ms. We assumed that $G_A = G_{Kdr}$, consistently with experimental
794 data (see S8 Fig A).

795

796 ***Numerical simulations and dynamical systems analysis***

797 We integrated numerically the deterministic model using the freeware XPPAUT
798 (Ermentrout 2002) and a standard fourth-order Runge-Kutta algorithm. XPPAUT was also
799 used to compute one-parameter and two-parameters bifurcation diagrams. The stochastic
800 version of the model was also implemented in XPPAUT and computed with a Gillespie's
801 algorithm (Gillespie 1976).

802 To investigate the dynamics of the model with slow inactivation of I_{Nap}, we relied on
803 numerical simulations together with fast/slow dynamics analysis (Witelski & Bowen 2015).

804 In this approach, one distinguishes slow dynamical variables (here only s) and fast dynamical
805 variables. Slow variables vary little at the time scale of fast variables and may therefore be
806 considered as constant parameters of the fast dynamics in first approximation. In contrast,
807 slow variables are essentially sensitive to the time average of the fast variables, much more
808 than to their instantaneous values. This separation of time scales allows one to conduct a
809 phase plane analysis of the full dynamics.

810
811 ***Statistics***

812 All values were expressed as mean ± SEM. Statistical significance was assessed by non-
813 parametric Kruskal-Wallis test with Dunn's post hoc test, Mann-Whitney test or Wilcoxon
814 matched pairs test (GraphPad Prism 5.0 Software, USA). Significant changes in the
815 proportions of firing patterns with age were assessed by chi-square test for large sample and
816 by Fisher's exact test for small sample. Significance was determined at $P < 0.05$.

Acknowledgments

We thank Susanne Bolte, Jean-François Gilles and France Lam for assistance with confocal imaging (IBPS imaging facility) and IBPS rodent facility team for animal care and production. We thank University Paris Descartes for hosting Yulia Timofeeva as an invited professor. This work was supported by INSERM, CNRS, Sorbonne Université (Paris), Université de Bordeaux, Université Paris Descartes and Fondation pour la Recherche Médicale.

Declaration of Interests

The authors declare no competing interests

827 # References

828 Allain AE, Bairi A, Meyrand P, Branchereau P. 2004. Ontogenic changes of the GABAergic
829 system in the embryonic mouse spinal cord. *Brain research* 1000: 134-47
830 Allain AE, Le Corronc H, Delpy A, Cazenave W, Meyrand P, et al. 2011. Maturation of the
831 GABAergic transmission in normal and pathologic motoneurons. *Neural plasticity*
832 2011: 905624
833 Allain AE, Segu L, Meyrand P, Branchereau P. 2010. Serotonin controls the maturation of the
834 GABA phenotype in the ventral spinal cord via 5-HT1b receptors. *Annals of the New*
835 *York Academy of Sciences* 1198: 208-19
836 Alvarez FJ, Benito-Gonzalez A, Siembab VC. 2013. Principles of interneuron development
837 learned from Renshaw cells and the motoneuron recurrent inhibitory circuit. *Annals of*
838 *the New York Academy of Sciences* 1279: 22-31
839 Angelim M, Maia L, Mouffle C, Ginhoux F, Low D, et al. 2018. Embryonic macrophages and
840 microglia ablation alter the development of dorsal root ganglion sensory neurons in
841 mouse embryos. *Glia* 66: 2470-86
842 Baer SM, Erneux T, Rinzel J. 1989. The Slow Passage through a Hopf Bifurcation: Delay,
843 Memory Effects, and Resonance
844 . *SIAM Journal on Applied Mathematics* 49: 55-71
845 Ballion B, Branchereau P, Chapron J, Viala D. 2002. Ontogeny of descending serotonergic
846 innervation and evidence for intraspinal 5-HT neurons in the mouse spinal cord. *Brain*
847 *research. Developmental brain research* 137: 81-8
848 Belleau ML, Warren RA. 2000. Postnatal development of electrophysiological properties of
849 nucleus accumbens neurons. *Journal of neurophysiology* 84: 2204-16
850 Benito-Gonzalez A, Alvarez FJ. 2012. Renshaw cells and Ia inhibitory interneurons are
851 generated at different times from p1 progenitors and differentiate shortly after exiting
852 the cell cycle. *J Neurosci* 32: 1156-70
853 Bertram R, Butte MJ, Kiemel T, Sherman A. 1995. Topological and phenomenological
854 classification of bursting oscillations. *Bulletin of mathematical biology* 57: 413-39
855 Bikoff JB, Gabitto MI, Rivard AF, Drobac E, Machado TA, et al. 2016. Spinal Inhibitory
856 Interneuron Diversity Delineates Variant Motor Microcircuits. *Cell* 165: 207-19
857 Blankenship AG, Feller MB. 2010. Mechanisms underlying spontaneous patterned activity in
858 developing neural circuits. *Nature reviews. Neuroscience* 11: 18-29

859 Boeri J, Le Corronc H, Lejeune FX, Le Bras B, Mouffle C, et al. 2018. Persistent Sodium
860 Current Drives Excitability of Immature Renshaw Cells in Early Embryonic Spinal
861 Networks. *J Neurosci* 38: 7667-82
862 Borisyuk A, Rinzel J. 2005. Understanding neuronal dynamics by geometrical dissection of
863 minimal models In *Models and Methods in Neurophysics*, ed. C Chow, B Gutkin, D
864 Hansel, C Meunier, J Dalibard, pp. 19-72. Proc Les Houches Summer School 2003,
865 (Session LXXX): Elsevier
866 Branchereau P, Chapron J, Meyrand P. 2002. Descending 5-hydroxytryptamine raphe inputs
867 repress the expression of serotonergic neurons and slow the maturation of inhibitory
868 systems in mouse embryonic spinal cord. *J Neurosci* 22: 2598-606
869 Branchereau P, Morin D, Bonnot A, Ballion B, Chapron J, Viala D. 2000. Development of
870 lumbar rhythmic networks: from embryonic to neonate locomotor-like patterns in the
871 mouse. *Brain research bulletin* 53: 711-8
872 Chevalier M, Toporikova N, Simmers J, Thoby-Brisson M. 2016. Development of pacemaker
873 properties and rhythmogenic mechanisms in the mouse embryonic respiratory network.
874 *eLife* 5
875 Coetzee WA, Amarillo Y, Chiu J, Chow A, Lau D, et al. 1999. Molecular diversity of K+
876 channels. *Annals of the New York Academy of Sciences* 868: 233-85
877 Crill WE. 1996. Persistent sodium current in mammalian central neurons. *Annual review of*
878 *physiology* 58: 349-62
879 Czarnecki A, Le Corronc H, Rigato C, Le Bras B, Couraud F, et al. 2014. Acetylcholine
880 controls GABA-, glutamate-, and glycine-dependent giant depolarizing potentials that
881 govern spontaneous motoneuron activity at the onset of synaptogenesis in the mouse
882 embryonic spinal cord. *J Neurosci* 34: 6389-404
883 Delpy A, Allain AE, Meyrand P, Branchereau P. 2008. NKCC1 cotransporter inactivation
884 underlies embryonic development of chloride-mediated inhibition in mouse spinal
885 motoneuron. *J Physiol* 586: 1059-75
886 Durand J, Filipchuk A, Pambo-Pambo A, Amendola J, Borisovna Kulagina I, Gueritaud JP.
887 2015. Developing electrical properties of postnatal mouse lumbar motoneurons.
888 *Frontiers in cellular neuroscience* 9: 349
889 Eccles JC, Fatt P, Landgren S. 1956. The inhibitory pathway to motoneurones. *Progress in*
890 *neurobiology*: 72-82

Ermentrout B. 2002. *Simulating, Analyzing, and Animating Dynamical Systems: A Guide to XPPAUT for Researchers and Students*. pp. xiii + 298. Philadelphia: Society for Industrial and Applied Mathematics.

Gao BX, Ziskind-Conhaim L. 1998. Development of ionic currents underlying changes in action potential waveforms in rat spinal motoneurons. *Journal of neurophysiology* 80: 3047-61

Gao H, Lu Y. 2008. Early development of intrinsic and synaptic properties of chicken nucleus laminaris neurons. *Neuroscience* 153: 131-43

Gillespie DT. 1976. A general method for numerically simulating the stochastic time evolution of coupled chemical reactions. *Journal of Computational Physics* 22: 403-34

Gutman GA, Chandy KG, Grissmer S, Lazdunski M, McKinnon D, et al. 2005. International Union of Pharmacology. LIII. Nomenclature and molecular relationships of voltage-gated potassium channels. *Pharmacological reviews* 57: 473-508

Hallermann S, Silver RA. 2013. Sustaining rapid vesicular release at active zones: potential roles for vesicle tethering. *Trends in neurosciences* 36: 185-94

Hanson MG, Landmesser LT. 2003. Characterization of the circuits that generate spontaneous episodes of activity in the early embryonic mouse spinal cord. *J Neurosci* 23: 587-600

Hanson MG, Landmesser LT. 2004. Normal patterns of spontaneous activity are required for correct motor axon guidance and the expression of specific guidance molecules. *Neuron* 43: 687-701

Hanson MG, Landmesser LT. 2006. Increasing the frequency of spontaneous rhythmic activity disrupts pool-specific axon fasciculation and pathfinding of embryonic spinal motoneurons. *J Neurosci* 26: 12769-80

Hanson MG, Milner LD, Landmesser LT. 2008. Spontaneous rhythmic activity in early chick spinal cord influences distinct motor axon pathfinding decisions. *Brain Res Rev* 57: 77-85

Henley J, Poo MM. 2004. Guiding neuronal growth cones using Ca2+ signals. *Trends in cell biology* 14: 320-30

Holden S, Erneux T. 1993. Slow Passage Through a Hopf Bifurcation: From Oscillatory to Steady State Solutions. ***SIAM Journal on Applied Mathematics*** 53: 1045-58

Huang H, Trussell LO. 2008. Control of presynaptic function by a persistent Na(+) current. *Neuron* 60: 975-9

924 Izhikevich EM. 2000a. Neural excitability, spiking and bursting. *Int. J. Bifurcation Chaos* 10:
925 1171-266
926 Izhikevich EM. 2000b. Subcritical Elliptic Bursting of Bautin Type. *SIAM Journal on Applied*
927 *Mathematics* 60: 503-35
928 Katz LC, Shatz CJ. 1996. Synaptic activity and the construction of cortical circuits. *Science*
929 274: 1133-8
930 Khazipov R, Luhmann HJ. 2006. Early patterns of electrical activity in the developing
931 cerebral cortex of humans and rodents. *Trends in neurosciences* 29: 414-18
932 Kole MH, Stuart GJ. 2012. Signal processing in the axon initial segment. *Neuron* 73: 235-47
933 Kuo JJ, Lee RH, Zhang L, Heckman CJ. 2006. Essential role of the persistent sodium current
934 in spike initiation during slowly rising inputs in mouse spinal neurones. *J Physiol* 574:
935 819-34
936 Liu SJ, Kaczmarek LK. 1998. The expression of two splice variants of the Kv3.1 potassium
937 channel gene is regulated by different signaling pathways. *J Neurosci* 18: 2881-90
938 Liu X, Pfaff DW, Calderon DP, Tabansky I, Wang X, et al. 2016. Development of
939 Electrophysiological Properties of Nucleus Gigantocellularis Neurons Correlated with
940 Increased CNS Arousal. *Developmental neuroscience* 38: 295-310
941 Marcotti W, Johnson SL, Holley MC, Kros CJ. 2003a. Developmental changes in the
942 expression of potassium currents of embryonic, neonatal and mature mouse inner hair
943 cells. *J Physiol* 548: 383-400
944 Marcotti W, Johnson SL, Rusch A, Kros CJ. 2003b. Sodium and calcium currents shape
945 action potentials in immature mouse inner hair cells. *J Physiol* 552: 743-61
946 Marmigere F, Ernfors P. 2007. Specification and connectivity of neuronal subtypes in the
947 sensory lineage. *Nature reviews. Neuroscience* 8: 114-27
948 McKay BE, Turner RW. 2005. Physiological and morphological development of the rat
949 cerebellar Purkinje cell. *J Physiol* 567: 829-50
950 Milner LD, Landmesser LT. 1999. Cholinergic and GABAergic inputs drive patterned
951 spontaneous motoneuron activity before target contact. *J Neurosci* 19: 3007-22
952 Momose-Sato Y, Sato K. 2013. Large-scale synchronized activity in the embryonic brainstem
953 and spinal cord. *Frontiers in cellular neuroscience* 7: 36
954 Moody WJ, Bosma MM. 2005. Ion channel development, spontaneous activity, and activity-
955 dependent development in nerve and muscle cells. *Physiological reviews* 85: 883-941

956 Myers CP, Lewcock JW, Hanson MG, Gosgnach S, Aimone JB, et al. 2005. Cholinergic input
957 is required during embryonic development to mediate proper assembly of spinal
958 locomotor circuits. *Neuron* 46: 37-49
959 O'Donovan MJ. 1999. The origin of spontaneous activity in developing networks of the
960 vertebrate nervous system. *Curr Opin Neurobiol* 9: 94-104
961 Osinga HM, Sherman A, Tsaneva-Atanasova K. 2012. Cross-Currents between Biology and
962 Mathematics: The Codimension of Pseudo-Plateau Bursting. *Discrete and continuous*
963 *dynamical systems. Series A* 32: 2853-77
964 Osinga HM, Tsaneva-Atanasova KT. 2010. Dynamics of plateau bursting depending on the
965 location of its equilibrium. *Journal of neuroendocrinology* 22: 1301-14
966 Oster A, Faure P, Gutkin BS. 2015. Mechanisms for multiple activity modes of VTA
967 dopamine neurons. *Frontiers in computational neuroscience* 9: 95
968 Ozaki S, Snider WD. 1997. Initial trajectories of sensory axons toward laminar targets in the
969 developing mouse spinal cord. *The Journal of comparative neurology* 380: 215-29
970 Perry S, Gezelius H, Larhammar M, Hilscher MM, Lamotte d'Incamps B, et al. 2015. Firing
971 properties of Renshaw cells defined by Chrna2 are modulated by hyperpolarizing and
972 small conductance ion currents Ih and ISK. *The European journal of neuroscience* 41:
973 889-900
974 Picken Bahrey HL, Moody WJ. 2003. Early development of voltage-gated ion currents and
975 firing properties in neurons of the mouse cerebral cortex. *Journal of neurophysiology*
976 89: 1761-73
977 Pineda R, Ribera A. 2010. Evolution of the Action Potential In *Evolution of Nervous Systems*,
978 ed. JH Kaas, pp. 211-38: Elsevier Ltd
979 Prasad T, Wang X, Gray PA, Weiner JA. 2008. A differential developmental pattern of spinal
980 interneuron apoptosis during synaptogenesis: insights from genetic analyses of the
981 protocadherin-gamma gene cluster. *Development* 135: 4153-64
982 Pun S, Sigrist M, Santos AF, Ruegg MA, Sanes JR, et al. 2002. An intrinsic distinction in
983 neuromuscular junction assembly and maintenance in different skeletal muscles.
984 *Neuron* 34: 357-70
985 Ramoa AS, McCormick DA. 1994. Developmental changes in electrophysiological properties
986 of LGNd neurons during reorganization of retinogeniculate connections. *J Neurosci*
987 14: 2089-97

988 Rigato C, Buckinx R, Le-Corronc H, Rigo JM, Legendre P. 2011. Pattern of invasion of the
989 embryonic mouse spinal cord by microglial cells at the time of the onset of functional
990 neuronal networks. *Glia* 59: 675-95
991 Rinzel J. 1985. Bursting oscillations in an excitable membrane model In *Ordinary and*
992 *Partial Differential Equations. Lecture Notes in Mathematics*, ed. B Sleeman, R Jarvis,
993 pp. 304–16. Berlin, Heidelberg: Springer
994 Rousseeuw PJ. 1987. Silhouettes - a Graphical Aid to the Interpretation and Validation of
995 Cluster-Analysis. *J Comput Appl Math* 20: 53-65
996 Saint-Amant L. 2010. Development of motor rhythms in zebrafish embryos. *Progress in*
997 *brain research* 187: 47-61
998 Sapir T, Geiman EJ, Wang Z, Velasquez T, Mitsui S, et al. 2004. Pax6 and engrailed 1
999 regulate two distinct aspects of renshaw cell development. *J Neurosci* 24: 1255-64
1000 Scain AL, Le Corronc H, Allain AE, Muller E, Rigo JM, et al. 2010. Glycine release from
1001 radial cells modulates the spontaneous activity and its propagation during early spinal
1002 cord development. *J Neurosci* 30: 390-403
1003 Sigworth FJ, Sine SM. 1987. Data transformations for improved display and fitting of single-
1004 channel dwell time histograms. *Biophysical journal* 52: 1047-54
1005 Sillar KT, Simmers AJ, Wedderburn JF. 1992. The post-embryonic development of cell
1006 properties and synaptic drive underlying locomotor rhythm generation in Xenopus
1007 larvae. *Proceedings. Biological sciences* 249: 65-70
1008 Song ZM, Hu J, Rudy B, Redman SJ. 2006. Developmental changes in the expression of
1009 calbindin and potassium-channel subunits Kv3.1b and Kv3.2 in mouse Renshaw cells.
1010 *Neuroscience* 139: 531-8
1011 Sontheimer H, Trotter J, Schachner M, Kettenmann H. 1989. Channel expression correlates
1012 with differentiation stage during the development of oligodendrocytes from their
1013 precursor cells in culture. *Neuron* 2: 1135-45
1014 Spitzer NC. 2006. Electrical activity in early neuronal development. *Nature* 444: 707-12
1015 Spitzer NC, Vincent A, Lautermilch NJ. 2000. Differentiation of electrical excitability in
1016 motoneurons. *Brain research bulletin* 53: 547-52
1017 Stam FJ, Hendricks TJ, Zhang J, Geiman EJ, Francius C, et al. 2012. Renshaw cell
1018 interneuron specialization is controlled by a temporally restricted transcription factor
1019 program. *Development* 139: 179-90

1020 Stern JV, Osinga HM, LeBeau A, Sherman A. 2008. Resetting behavior in a model of
1021 bursting in secretory pituitary cells: distinguishing plateaus from pseudo-plateaus.
1022 *Bulletin of mathematical biology* 70: 68-88
1023 Su J, Rubin J, Terman D. 2004. Effects of noise on elliptic bursters. *Nonlinearity* 17: 133-57
1024 Taddese A, Bean BP. 2002. Subthreshold sodium current from rapidly inactivating sodium
1025 channels drives spontaneous firing of tuberomammillary neurons. *Neuron* 33: 587-600
1026 Tagliavini A, Tabak J, Bertram R, Pedersen MG. 2016. Is bursting more effective than
1027 spiking in evoking pituitary hormone secretion? A spatiotemporal simulation study of
1028 calcium and granule dynamics. *American journal of physiology. Endocrinology and*
1029 *metabolism* 310: E515-25
1030 Tamamaki N, Yanagawa Y, Tomioka R, Miyazaki J, Obata K, Kaneko T. 2003. Green
1031 fluorescent protein expression and colocalization with calretinin, parvalbumin, and
1032 somatostatin in the GAD67-GFP knock-in mouse. *The Journal of comparative*
1033 *neurology* 467: 60-79
1034 Teka W, Tsaneva-Atanasova K, Bertram R, Tabak J. 2011. From plateau to pseudo-plateau
1035 bursting: making the transition. *Bulletin of mathematical biology* 73: 1292-311
1036 Tibbs GR, Barrie AP, Van Mieghem FJ, McMahon HT, Nicholls DG. 1989. Repetitive action
1037 potentials in isolated nerve terminals in the presence of 4-aminopyridine: effects on
1038 cytosolic free Ca2+ and glutamate release. *Journal of neurochemistry* 53: 1693-9
1039 Tong H, McDearmid JR. 2012. Pacemaker and plateau potentials shape output of a
1040 developing locomotor network. *Current biology : CB* 22: 2285-93
1041 Tsaneva-Atanasova K, Osinga HM, Riess T, Sherman A. 2010. Full system bifurcation
1042 analysis of endocrine bursting models. *Journal of theoretical biology* 264: 1133-46
1043 Vinay L, Brocard F, Clarac F. 2000. Differential maturation of motoneurons innervating ankle
1044 flexor and extensor muscles in the neonatal rat. *The European journal of neuroscience*
1045 12: 4562-6
1046 Wang LY, Kaczmarek LK. 1998. High-frequency firing helps replenish the readily releasable
1047 pool of synaptic vesicles. *Nature* 394: 384-8
1048 Witelski T, Bowen M. 2015. *Fast/slow Dynamical Systems. In: Methods of Mathematical*
1049 *Modelling*. pp. 201-213. Springer, Cham.
1050 Yvert B, Branchereau P, Meyrand P. 2004. Multiple spontaneous rhythmic activity patterns
1051 generated by the embryonic mouse spinal cord occur within a specific developmental
1052 time window. *Journal of neurophysiology* 91: 2101-9
1053

Figure captions

Figure 1. Delayed Rectifier and A-Type potassium currents are present in embryonic V1^{R} at E12.5

(A) Representative traces of voltage responses showing single-spiking activity (left trace), repetitive action potential firing (middle trace) and plateau potential activity (right trace). (B1, B2 and B3) Representative examples of the total outward K^+ currents obtained from V_H = -100 mV (left traces), of I_{Kdr} (V_H = -30 mV, middle traces) and of isolated I_A (left traces) recorded at E12.5 in SS V1^{R} (A1), RS V1^{R} (A2) and PP V1^{R} (B3). Voltage-dependent potassium currents were evoked in response to 10 mV membrane potential steps (200 ms) from -100 or from -30 mV to +40 mV (10 s interval between pulses). V1^{R} were voltage clamped at V_H = -60 mV. A prepulse of -40 mV (300 ms) was applied to activate both I_A and I_{Kdr}. I_{Kdr} was isolated by applying a prepulse of 30 mV (300 ms) to inactivate I_A (B1 insert). I_A was isolated by subtracting step-by-step the currents obtained using a prepulse of 30 mV (V_H = - 30 mV) from the currents obtained using a prepulse of -40 mV (V_H = -100 mV). (C1, C2 and C3) Current-voltage relationship ($I-V$ curves) of I_{Kdr} (filled circles) and of I_A (open circles) recorded in SS V1^{R} (C1), RS V1^{R} (C2) and PP V1^{R} (C3). $I-V$ curves were obtained from currents shown in A1, A2 and A3. Note that the $I-V$ curves are similar between SS V1^{R}, RS V1^{R}, PP V1^{R}.

Figure 2. Maximal G_{Kdr}, G_{Nap} values and G_{Nap}/G_{Kdr} ratio in embryonic V1^{R} recorded at E12.5 and at E14.5

(A) Bar graph showing maximal G_{Kdr} value (Max G_{Kdr}) in SS V1^{R} at E12.5 (n = 9; gray bar) and at E14.5 (n = 10; gray bar), and in RS V1^{R} (n = 7; red bar), ME V1^{R} (n = 3; purple bar) and PP V1^{R} at E12.5 (n = 7; blue bar). G_{Kdr} was calculated from I_{Kdr} at V_H = + 20 mV, assuming a K^+ equilibrium potential of -96 mV. There is no significant difference

in G_{Kdr} between SS V1^R and RS V1^R, while G_{Kdr} is significantly smaller in PP V1^R as compared to SS V1^R and RS V1^R. G_{Kdr} was significantly higher in SS V1^R at E14.5 than in SS V1^R, RS V1^R and PP V1^R at E12.5. (Kruskall-Wallis test $P < 0.0001$; SS V1^R versus RS V1^R at E12.5, $P = 0.5864$; SS V1^R versus PP V1^R at E12.5, $P = 0.0243$; RS V1^R versus PP V1^R at E12.5, $P = 0.0086$; E14.5 SS V1^R versus E12.5 SS V1^R, $P = 0.0048$; E14.5 SS V1^R versus E12.5 RS V1^R, $P = 0.0384$, E14.5 SS V1^R versus E12.5 PP V1^R, $P < 0.0001$). The increase in G_{Kdr} between E12.5 and E14.5 is likely to be due to the increase in neuronal size (input capacitance; Figure 2A). Indeed there was no significant difference (Mann Whitney test, $P = 0.133$) in G_{Kdr} density between SS V1^R at E12.5 (408.5 ± 42.95 pS/pF, n = 9) and at E14.5 (522.6 ± 49.6 pS/pF, n = 10). (B) Bar graph showing the maximal G_{Nap} value (Max G_{Nap}) in SS V1^R at E12.5 (n 9; gray bar) and E14.5 (n = 10; green bar), and in RS V1^R (n = 8; red bar), ME V1^R (n = 3; purple bar) and PP V1^R (n = 6; blue bar) at E12.5. Max G_{Nap} was calculated from maximal I_{Nap} value measured on current evoked by assuming a Na^+ equilibrium potential of +60 mV. There was no difference in G_{Nap} between RS V1^R and PP V1^R. On the contrary, G_{Nap} measured in SS V1^R at E12.5 or at E14.5 was significantly smaller as compared to G_{Nap} measured at E12.5 in RS V1^R or in PP V1^R. G_{Nap} measured at E12.5 and E14.5 in SS V1^R were not significantly different (Kruskall-Wallis test $P < 0.0001$; E12.5 SS V1^R versus E12.5 RS V1^R, $P = 0.0034$; E12.5 SS V1^R versus E12.5 PP V1^R, $P = 0.0006$; E12.5 RS V1^R versus E12.5 PP V1^R, $P = 0.5494$; E14.5 SS V1^R versus E12.5 SS V1^R, $P = 0.5896$; E14.5 SS V1^R versus E12.5 RS V1^R, $P = 0.0005$; E14.5 SS V1^R versus E12.5 PP V1^R, $P < 0.0001$). (C) Histograms showing the G_{Nap} / G_{Kdr} ratio in SS V1^R at E12.5 (n = 9; gray bar) and E14.5 (n = 10; green bar) and in RS V1^R (n = 8; red bar), ME V1^R (n = 3; purple bar) and PP V1^R (n = 6; blue bar) at E12.5. Note that the G_{Nap} / G_{Kdr} ratio differs significantly between SS V1^R, RS V1^R and PP V1^R at E12.5, while it is not different between SS V1^R recorded at E12.5 and at E14.5 (Kruskall-Wallis test $P < 0.0001$; SS V1^R versus RS V1^R at

E12.5, P = 0.0367; SS V1^R versus PP V1^R at E12.5, P < 0.0001; RS V1^R versus PP V1^R at E12.5, P = 0.0159; E14.5 SS V1^R versus E12.5 SS V1^R, P = 0.2319; E14.5 SS V1^R versus E12.5 RS V1^R, P = 0.0017; E14.5 SS V1^R versus E12.5 PP V1^R P < 0.0001). Data shown in A and B were used to calculate G_{Nap} / G_{Kdr} ratio shown in C. (*P < 0.05, ** P < 0.01, *** P < 0.001).

Figure 3. Delayed Rectifier potassium current was inhibited by low concentrations of 4-aminopyridine in embryonic V1^R recorded at E12.5

Example of voltage-dependent potassium currents evoked in response to 10 mV membrane potential steps (200 ms) from -100 mV or from -30 mV to +40 mV (10 s interval between pulses). V1 ^{R} were voltage clamped at V_H = -60 mV. A prepulse of -40 mV (300 ms) was applied to activate both I_A and I_{Kdr}. I_{Kdr} was evoked in response to 10 mV membrane potential steps (200 ms) from -100 mV to +40 mV. V1 ^{R} were voltage clamped at V_H = -60 mV. A prepulse of 30 mV (V_H = - 30 mV) was applied to isolate I_{Kdr}. (A1) Representative example of the effect of 300 μM 4-AP application on I_{Kdr} recorded from embryonic V1^R at E12.5. (A2) Curves showing current-voltage relationships of I_{Kdr} in control and in the presence of 300 μM 4-AP. Measurements were performed on traces shown in A1. (B) Dose-response relationship of 4-AP-evoked I_{Kdr} inhibition (mean + SE). Data were normalized to I_{Kdr} amplitude measured in the absence of 4-AP (V_H = 40mV) and fitted as explained in Materials and Methods. Note that 4-AP IC_{50} is in μM range (2.9 μM). 0.3 μM 4-AP n = 3, 1 μM 4-AP n = 3, 3 μM 4-AP n = 9, 10 μM 4-AP n = 13, 30 μM 4-AP n = 7, 100 μM 4-AP n = 7, 300 μM 4-AP n = 7.

Figure 4. Increasing 4-AP concentration changed the firing pattern of single spiking embryonic V1^R recorded at E12.5

1128 The firing pattern of embryonic $V1^R$ was evoked by 2 s suprathreshold depolarizing current
1129 steps. (A1-A2) Representative traces showing examples of the effect of increasing
1130 concentration of 4-AP (from 3 to 300 µM) on the firing pattern of a SS $V1^R$ recorded at E12.5.
1131 Note that in this case increasing 4-AP concentration converted single spiking (black trace) to
1132 repetitive spiking (red trace), repetitive spiking to a mixed event pattern (purple trace) and
1133 mixed events to plateau potential (blue trace). (A2) Example of SS $V1^R$ in which increasing 4-
1134 AP concentration converted single spiking to repetitive spiking only. (A3) Bar plots showing
1135 the change in the firing pattern of SS $V1^R$ according to 4-AP concentrations (control n = 10, 3
1136 µM 4-AP n = 8, 10 µM 4-AP n = 10, 30 µM 4-AP n = 10, 100 µM 4-AP n = 10, 300 µM 4-AP
1137 n = 8). (B) Representative traces showing the effect of 0.5 µM TTX on a plateau potential
1138 evoked in a SS $V1^R$ in the presence of 300 µM 4-AP. (C) Representative traces showing the
1139 effect of 0.5 µM TTX on repetitive AP firing evoked in a SS $V1^R$ in the presence of 300 µM
1140 4-AP. In both cases, the application of TTX fully blocked the responses evoked in the
1141 presence of 4-AP, indicating that they were underlain by the activation of voltage-gated Na^+
1142 channels.
1143
1144 **Figure 5. Cluster analysis of embryonic $V1^R$ firing pattern in the embryonic spinal cord**
1145 **at E12.5**
1146 (A, inserts) Cluster analysis of embryonic $V1^R$ firing pattern was performed using three
1147 parameters that describe the firing pattern during a 2 s suprathreshold depolarizing pulses: the
1148 mean of the half-amplitude event duration (mean ½Ad), the coefficient of variation of ½ Ad
1149 (CV ½Ad) allowing to quantify the AP variation within a train (CV was set to 0 when the
1150 number of spikes evoked by a depolarizing pulse was ≤ 3) and the duration ratio ddr = Σ½
1151 Ad/Pw, obtained by dividing the sum of ½ Ad by the pulse duration Pw, that indicates the
1152 total time spent in the depolarized state. For example, ddr = 1 when a plateau potential lasts as

long as the depolarizing pulse. Conversely, its value is low when the depolarizing pulse evokes a single AP only. A. Dendrogram for complete linkage hierarchical clustering of 163 embryonic $V1^R$ according to the values of log mean ½Ad, of CV ½Ad and of log ddr. The colored matrix below the dendrogram shows the variations of these three parameters for all the cells in the clusters (colored trees) extracted from the dendrogram. (B) The number of clusters was determined by analyzing the distribution of silhouette width values (see Material and Methods). The boxplots show the distribution of silhouette width values when the number of clusters k varies from 2 to 12. The mean silhouette width values (red diamond shaped points) attained their maximum when the estimated cluster number was 5. (C) 3D plot showing cluster distribution of embryonic $V1^R$ according to log mean ½Ad, CV ½Ad and log ddr. Each cluster corresponds to a particular firing pattern as illustrated in D: $V1^R$ that cannot sustain repetitive firing of APs (1 to 3 AP/pulse only, gray), $V1^R$ that can fire tonically (red), $V1^R$ with a firing pattern characterized by a mix of APs and relatively short plateau potentials (dark purple), $V1^R$ with a firing pattern characterized by a mix of APs and relatively long plateau potentials (light purple) and $V1^R$ with evoked plateau potentials only (blue). The arrow in D indicates 3 misclassified $V1^R$ that could not sustain repetitive firing although they were assigned to the cluster of repetitively firing $V1^R$ (see text).

Figure 6. Changes in the input capacitance, the input resistance and the threshold values of embryonic $V1^R$ from E11.5 to E16.5

(A) Graph showing how the input capacitance C_{in} of $V1^R$ changes with embryonic age. C_{in} significantly increased between E12.5 or E13.5 and E14.5 (Kruskall-Wallis test $P < 0.0001$; E12.5 versus E11.5 $P = 0.258$, E12.5 versus E13.5 $P = 0.904$, E12.5 versus E14.5 $P < 0.0001$, E12.5 versus E15.5 $P < 0.0001$, E12.5 versus E16.5 $P < 0.0001$, E13.5 versus E14.5 $P < 0.0001$, E13.5 versus E15.5 $P < 0.0001$, E13.5 versus E16.5 $P < 0.0001$; E11.5 n = 31, E12.5

n = 267, E13.5 n = 43, E14.5 n = 61, E15.5 n = 16, E16.5 n = 30). (B) Graph showing how the input resistance R_{in} of $V1^R$ changes with embryonic age. R_{in} significantly increased between E12.5 or E14.5 and E15.5 (Kruskall-Wallis test $P < 0.0001$; E12.5 versus E11.5 $P > 0.999$, E12.5 versus E13.5 $P = 0.724$, E12.5 versus E14.5 $P > 0.999$, E12.5 versus E15.5 $P = 0.0004$, E12.5 versus E16.5 $P = 0.0005$, E14.5 versus E15.5 $P = 0.0019$, E14.5 versus E16.5 $P < 0.0058$; E11.5 n = 31, E12.5 n = 261, E13.5 n = 43, E14.5 n = 60, E15.5 n = 16, E16.5 n = 30). (C) Graph showing how the threshold of regenerative events (APs and plateau potentials) of $V1^R$ changes with embryonic age. The average threshold became significantly more hyperpolarized after E12.5 (Kruskall-Wallis test $P < 0.0001$; E12.5 versus E11.5 $P = 0.676$, E12.5 versus E13.5 $P = 0.0039$, E12.5 versus E14.5 $P < 0.0001$, E12.5 versus E15.5 $P < 0.0001$, E12.5 versus E16.5 $P < 0.0001$, E13.5 versus E14.5 $P > 0.999$, E13.5 versus E15.5 $P = 0.1398$, E13.5 versus E16.5 $P = 0.0013$; E14.5 versus E15.5 $P > 0.999$, E14.5 versus E16.5 $P = 0.0634$, E15.5 versus E16.5 $P > 0.999$; E11.5 n = 20, E12.5 n = 162, E13.5 n = 31, E14.5 n = 30, E15.5 n = 16, E16.5 n = 30). Yellow and purple bars below the graphs indicate the two important phases of the functional development of spinal cord networks. The first one is characterized by synchronized neuronal activity (SNA) and the second one is characterized by the emergence of a locomotor-like activity (see text). Note that changes in C_{in} and R_{in} occurred at the end of the first developmental phase. (*$P < 0.05$, ** $P < 0.01$, *** $P < 0.001$; control, E12.5).

Figure 7. Developmental changes of embryonic $V1^R$ firing patterns from E11.5 to E16.5

The intrinsic activation properties were analyzed using 2 s suprathreshold depolarizing current steps. (A-E) Representative traces of voltage responses showing SS $V1^R$ (black), RS $V1^R$ (red), ME $V1^R$ (purple) and PP $V1^R$ (blue) at E11.5 (A), E13.5 (B), E14.5 (C) E15.5 (D) and E16.5 (E). (F) Bar graph showing how the proportions of the different firing patterns

change from E11.5 to E16.5 (E11.5 n = 22, E12.5 n = 165, E13.5 n = 32, E14.5 n = 57, E15.5 n = 15, 16.5 n = 28). Yellow and purple bars below the graphs indicate the first and the second phase of functional embryonic spinal cord networks. The proportions of the different firing patterns significantly changed between E11.5 to E12.5 (Fisher's exact test, $P = 0.0052$) with a significant increase in the proportion of RS $V1^R$ (Fisher's exact test, $P = 0.0336$) and a significant decrease in the proportion of ME $V1^R$ (Fisher's exact test, $P = 0.01071$) at E12.5. Only two firing patterns (SS and RS) were observed after E13.5 and most embryonic $V1^R$ lost their ability to sustain tonic firing after E13.5. However, at E16.5 the proportion of RS $V1^R$ significantly increased at the expense of SS $V1^R$ when compared to E14.5 (Fisher's exact test, $P = 0.0112$), indicating that embryonic $V1^R$ began to recover the ability to sustain tonic firing after E15.5.

Figure 8. **Activated caspase-3 is not observed in embryonic $V1^R$ at E14.5**

Representative confocal image of the ventral part of an isolated lumbar spinal cord of E14.5 GAD67-eGFP mouse embryo showing immunostainings using antibodies against eGFP (A), FoxD3 (B) and activated Caspase 3 (aCaspace 3, C). (D) Superimposition of the three stainings shows that embryonic $V1^R$ (eGFP+ and FoxD3+) were not aCaspase 3 immunoreactive. (A1, B1, C1 and D1) Enlarged images from A, B and C showing that aCaspase 3 staining is localized in areas where eGFP and Foxd3 stainings were absent. (A2, B2, C2 and D2) Enlarged images from A, B and C showing that aCaspase 3 staining is absent in the area where $V1^R$ (eGFP+ and FoxD3+) are located. aCaspase 3 staining that did not co-localize with GAD67eGFP likely indicates MN developmental cell death (Rigato et al 2011).

Figure 9. 600 µM 4-AP changed the firing pattern of single spiking embryonic $V1^R$ recorded at E14.5

The firing pattern of embryonic $V1^R$ was evoked by 2 s suprathreshold depolarizing current steps. (A1, A2) Representative traces showing the effect of 4-AP application (600 µM) on the firing pattern of single SS $V1^R$ recorded at E14.5. Note that the applications of 600 µM 4-AP evoked either a plateau potential (A1) or repetitive AP firing (A2), both fully blocked by TTX. (B) Bar plots showing the proportions of the different firing patterns observed in the presence of 600 µM 4-AP versus control recorded in SS $V1^R$ at E14.5 (n = 14).

Figure 10. Embryonic $V1^R$ firing patterns predicted by computational modeling

(A) Firing patterns of 27 recorded cells, in which both G_{Nap} and G_{Kdr} were measured. Gray: SS, red: RS, blue: PP. The three purple points located at the boundary between the RS and PP regions correspond to mixed events (ME) where plateau potentials alternate with spiking episodes. Note that no cell exhibited low values of both G_{Nap} and G_{Kdr} (lower left), or large values of both conductances (upper right). (B) Bifurcation diagram of the deterministic model when G_{Kdr} is kept fixed to 2.5 nS or 10 nS while G_{Nap} is varied. G_{in} = 1 nS and I = 20 pA. For G_{Kdr} = 10 nS (i.e. in the top experimental range), the red curves indicate the maximal and minimal voltages achieved on the stable limit cycle associated with repetitive firing (solid lines) and on the unstable limit cycle (dashed lines). The fixed point of the model is indicated by a gray solid line when it corresponds to the stable quiescent state, a gray dashed line when it is unstable and a solid blue line when it corresponds to a stable plateau potential. The two HB corresponding to the change of stability of the quiescence state (HB_1, G_{Nap}= 0.95 nS) and of the voltage plateau (HB_2, G_{Nap}= 3.04 nS) are indicated, as well as the two SN bifurcations of limit cycles associated with the onset (SN_1, G_{Nap} = 0.58 nS) and offset (SN_2, G_{Nap}= 3.14 nS) of repetitive spiking as G_{Nap} is increased. For G_{Kdr} = 2.5 nS, the model does not display repetitive firing; it possesses a unique fixed point, which is always stable (blue-gray curve). The transition from quiescence to plateau is gradual with no intervening bifurcation.

Representative voltage traces of the three different activity patterns are shown: single spiking in response to a 2 s current pulse (gray, G_{Nap} = 0.1 nS, G_{Kdr} = 10 nS), repetitive spiking (red, G_{Nap} = 1.5 nS, G_{Kdr} = 10 nS) and plateau potential (blue, G_{Nap} = 1.5 nS, G_{Kdr} = 2.5 nS). Note that the plateau never outlasts the current pulse. (C) Bifurcation diagram when G_{Nap} is kept fixed at 1.5 nS and G_{Kdr} is varied (I = 20 pA). Same conventions as in B. Plateau potential is stable until point HB_2 (G_{Kdr} = 5.05 nS), repetitive firing can be observed between HB_2 and SN_1 (G_{Kdr} = 21.05 nS). The quiescent state is stable from point HB_1 (G_{Kdr} = 15.76 nS) onward. Increasing G_{Nap} by merely 10% from 1.5 to 1.65 nS makes the bifurcation HB_2 subcritical (not shown). This is because the RS-PP transition of the model occurs near a Bautin bifurcation (a.k.a. generalized HB) bifurcation, where the supercritical HB, subcritical HB and the SN bifurcation of limit cycles merge as shown in D (point B_2). (D) Two-parameters bifurcation diagram of the model in the G_{Nap} - G_{Kdr} plane (I = 20 pA). The black lines indicate the bifurcations HB_1 and HB_2. The red lines indicate the SN bifurcations of limit cycles SN_1 and SN_2. The shaded area indicates the region where repetitive firing can occur. The black squares B_1 and B_2 correspond to Bautin bifurcations where supercritical HB (occurring between B_1 and B_2), subcritical HB (occurring on the rest of the HB_1 and HB_2 lines) and the SN bifurcations of limit cycles SN_1 and SN_2 coalesce. Because the model is near a Bautin bifurcation, its behavior is little affected by the nature of the bifurcation HB_2. When HB_2 is subcritical, the bistability region between HB2 and SN_2 is narrow (see Fig 9, B and D) and action potentials keep a large amplitude until their disappearance at point HB_2 (see Fig 9B). When HB_2 is supercritical, the spike amplitude vanishes at HB_2 but the decay is very steep (see Fig 9C). Taking into account channel noise further softens the distinction between these two cases. The oblique lines correspond to three different values of the ratio G_{Nap}/G_{Kdr}: 0.03 (gray), 0.2 (red) and 0.5 (blue). Voltage traces on the right display the response to a 2 s current pulse when channel noise is taken into account for the three regimes: quiescence (top,

gray trace and dot in the diagram), repetitive firing (middle, red) and plateau potential (bottom, blue). They correspond to the three deterministic voltage traces shown in B. Note that the one-parameter bifurcation diagrams shown in B correspond to horizontal lines through points 1 and 2 (G_{Kdr} = 10 nS) and through point 3 (G_{Kdr} = 2.5 nS), respectively. The bifurcation diagram in C corresponds to a vertical line through point 2 and 3 (G_{Nap} = 1.5 nS). (E) Cumulative distribution function of the ratio G_{Nap}/G_{Kdr} for the four clusters shown in A, showing the sequencing SS (gray) → RS (red) → ME (purple, 3 cells only) → PP (blue) predicted by the two-parameters bifurcation diagram in D. The wide PP range, as compared to SS and RS, merely comes from the fact that G_{Kdr} is small for cells in this cluster. (F) The data points in A are superimposed on the two-parameters bifurcation diagram shown in D, demonstrating that our basic model accounts well for SS, RS and PP clusters (indicated with the same color code as in A). The bifurcation diagram is simplified compared to A, only the region where repetitive spiking is possible (i.e. between the lines SN_1 and SN_2 in A) being displayed (shaded area). Notice that 3 ME cells (purple dots) are located near the transition between the RS and PP regions (indicated here by the purple fringe along the SN_2 bifurcation line). The four arrows indicate the presumable evolution of G_{Nap} and G_{Kdr} for SS, RS, ME and PP cells between E12.5 and E14.5-15.5. G_{Nap} eventually decreases while G_{Kdr} keeps on increasing. G. Distribution of a sample of cells in the G_{Kdr} - G_{Kdr} plane at E14.5. All the cells are located well within the SS region far from bifurcation lines because of the decreased G_{Nap} compared to E12.5, the increased G_{Kdr}, and the shift of the RS region (shaded) due to capacitance increase (18 versus 13 pF).

Figure 11. Effects of the slow inactivation of I_{Nap} on firing patterns predicted by computational modeling

(A) Examples of repetitive plateaus (left) and mixed events (right) recorded in $V1^R$ at E12.5 during a 2 s current pulse. (B1) Current-voltage curve of the basic model (without slow inactivation of I_{Nap}, and without I_A or channel noise) for G_{Kdr} = 2.5 nS and for G_{Nap} = 1.7 nS (lower curve) and 2.5 nS (upper curve). G_{in} = 2.5 nS. Solid lines denote stable fixed points and dashed lines unstable ones. For G_{Nap} =1.7 nS, bistability between quiescence and plateau occurs between the SN bifurcations SN_1 (I = 2.1 pA) and SN_2 (I = 8.3 pA). When G_{Nap} is increased to 2.5 nS, that bistability region extends to the negative current range, which implies that once a plateau has been elicited, the model will stay in that stable state and not return to the resting state, even though current injection is switched off (see insert). B1 Insert. Voltage response to a 2 s current pulse of 8 pA for G_{Nap} = 2.5 nS. The resting state (gray dot on the lower curve in B1 is destabilized at pulse onset and a plateau is elicited (blue dot on the upper curve in B1). At pulse offset, the plateau is maintained, even though the injected current is brought back to zero, and channel noise is not sufficient to go back to the resting state. (B2) Domain of bistability between quiescence and plateau (shaded) in the I- G_{Nap} plane for G_{Kdr}= 2.5 nS. It is delimited by the two lines SN_1 and SN_2 where SN bifurcations of fixed points occur. Bistability requires that G_{Nap} exceeds 1.35 nS, and the domain of bistabilty enlarges as G_{Nap} is increased further. The two horizontal lines correspond to the two cases shown in B1: G_{Nap} =1.7 nS and 2.5 nS. (C) Behavior of the model when slow inactivation is incorporated (half-inactivation voltage V_s = -30 mV, steepness k_s= -5 mV). The bifurcation diagram of the basic model (without slow inactivation) for I = 8 pA (compared to 20 pA in Fig 9) and G_{Kdr} = 2.5 nS (same conventions as in Fig 9B) and the stable limit cycle (black solid curve) obtained when slow inactivation is added (voltage-independent time constant: 1 s) are superimposed. The limit cycle is comprised of four successive phases (see labels): 1) long plateau during which I_{Nap} slowly inactivates, 2) fast transition to the quiescent state, 3) repolarization episode during which I_{Nap} slowly deinactivates, 4) fast transition back to the

plateau. Each plateau starts with a full blown action potential (or a series of rapidly decaying spikelets). Note that the bifurcation HB is subcritical here (unstable limit cycle in red), at variance with square wave bursting (supercritical bifurcation and stable limit cycle); this is a characteristic feature of pseudo-plateau bursting. Voltage responses to a 2 s current pulse are shown on the right for different kinetics of slow inactivation. Top: voltage-independent time constant of 1 s, Middle: same with channel noise added to fast and slow gating variables, Bottom: time constant increases with membrane voltage from 100 ms to 1 s (midpoint: -30 mV, steepness: 15 mV). (D) Mixed events. The bifurcation diagram of the basic model for G_{Kdr} = 2.5 nS and I = 10 pA and the stable limit cycle obtained in the presence of slow inactivation (G_{Nap} = 2.5 nS, V_s = -20 mV, k_s = -15 mV, voltage-independent time constant: 1 s) are superimposed. Here again, the limit cycle is comprised of four successive phases (see labels): 1) slow inactivation of I_{Nap} that leads to the crossing of the bifurcation point HB_2 and the destabilization of the plateau potential, 2) fast transition to the spiking regime, 3) repetitive spiking during which I_{Nap} slowly de-inactivates, which leads to the crossing of the bifurcation point SN_2 and terminates the spiking episode, 4) fast transition back to the stable plateau potential. Voltage traces for a constant injected current (10 pA) are shown on the right and in the absence of any channel noise. Top: voltage-independent time constant of 1 s, Bottom: time constant increases with membrane voltage from 200 to 800 ms (same V_s and k_s as in C). Note that in C and D the first plateau lasts longer than the following ones, as in electrophysiological recordings of embryonic $V1^R$ cells displaying repetitive plateaus. This form of adaptation is caused by the slow inactivation of the persistent sodium current.

Figure 12. Effect of 4-AP application on evoked GABAergic GICs or GDPs recorded in MNs at E12.5.

(A) Drawing showing the cervical position of the stimulation electrode and the lumbar position of the recording electrode. (B1) Evoked Giant Inward Current (GIC) in the presence of 4 mM kynurenic acid in control condition, in the presence of 30 μM 4-AP and 300 μM 4-AP. (B2) Bar graph showing GIC amplitude (pA) and half-width (s) (*$P < 0.05$). 4-AP applied at concentrations of 30 μM or 300 μM significantly increased the amplitude (Wilcoxon test, $P = 0.016$ and $P = 0.047$ respectively) and half-width (Wilcoxon test, $P = 0.016$ and $P = 0.018$ respectively) of GABAergic GIC. (C1) Evoked Giant Depolarizing Potential (GDP) in the presence of 4 mM kynurenic acid in control condition, in the presence of 30 μM 4-AP and 300 μM 4-AP. (C2) Bar graph showing GDPs amplitude (mV) and half-width (s). 4-AP applied at concentrations of 30 μM or 300 μM significantly increased GABAergic GDPs half-width (Wilcoxon test $P = 0.004$ and $P = 0.007$ respectively), but it did not significant change the amplitude (Wilcoxon test $P = 0.07$ and $P = 0.07$ respectively).

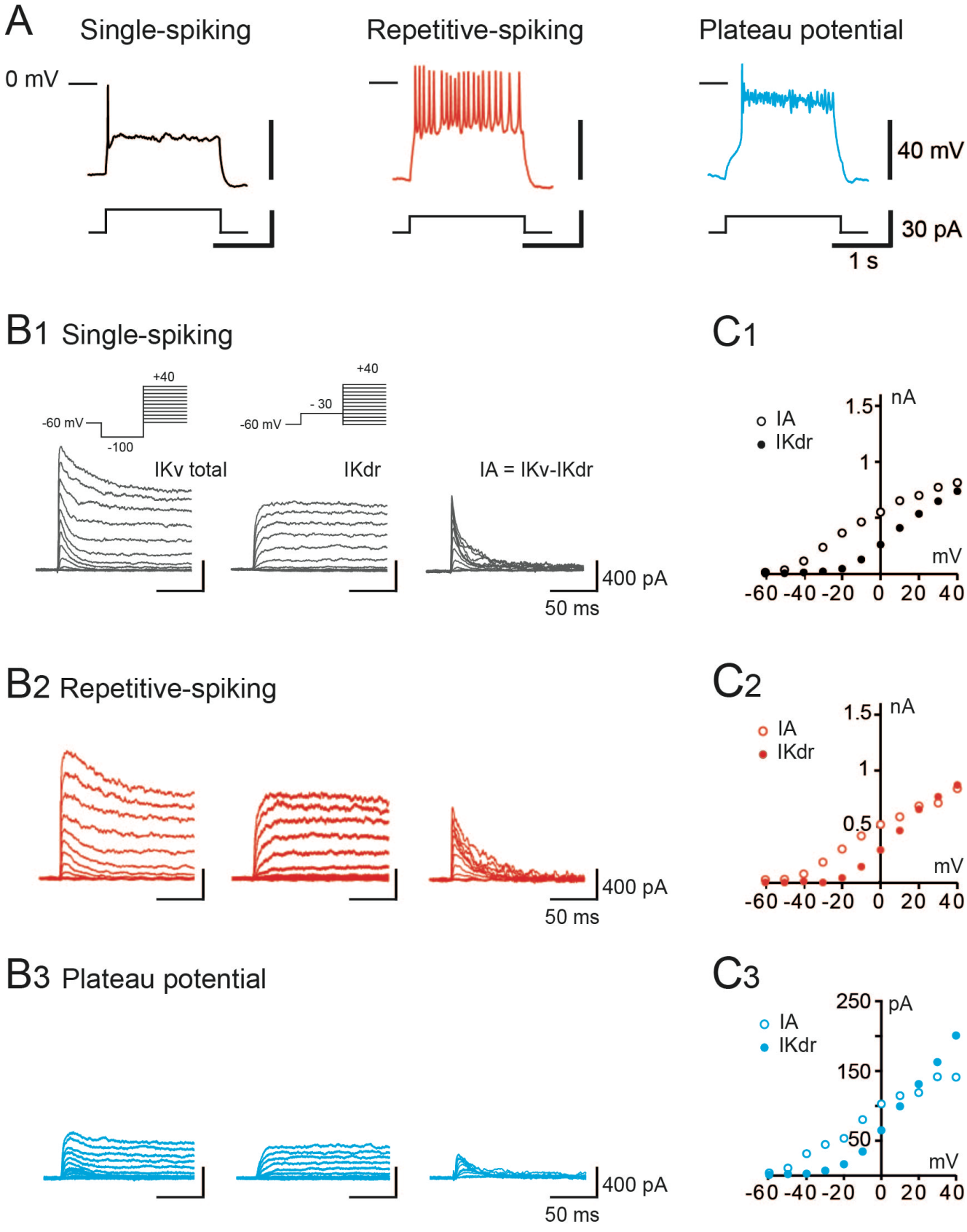

Figure 1

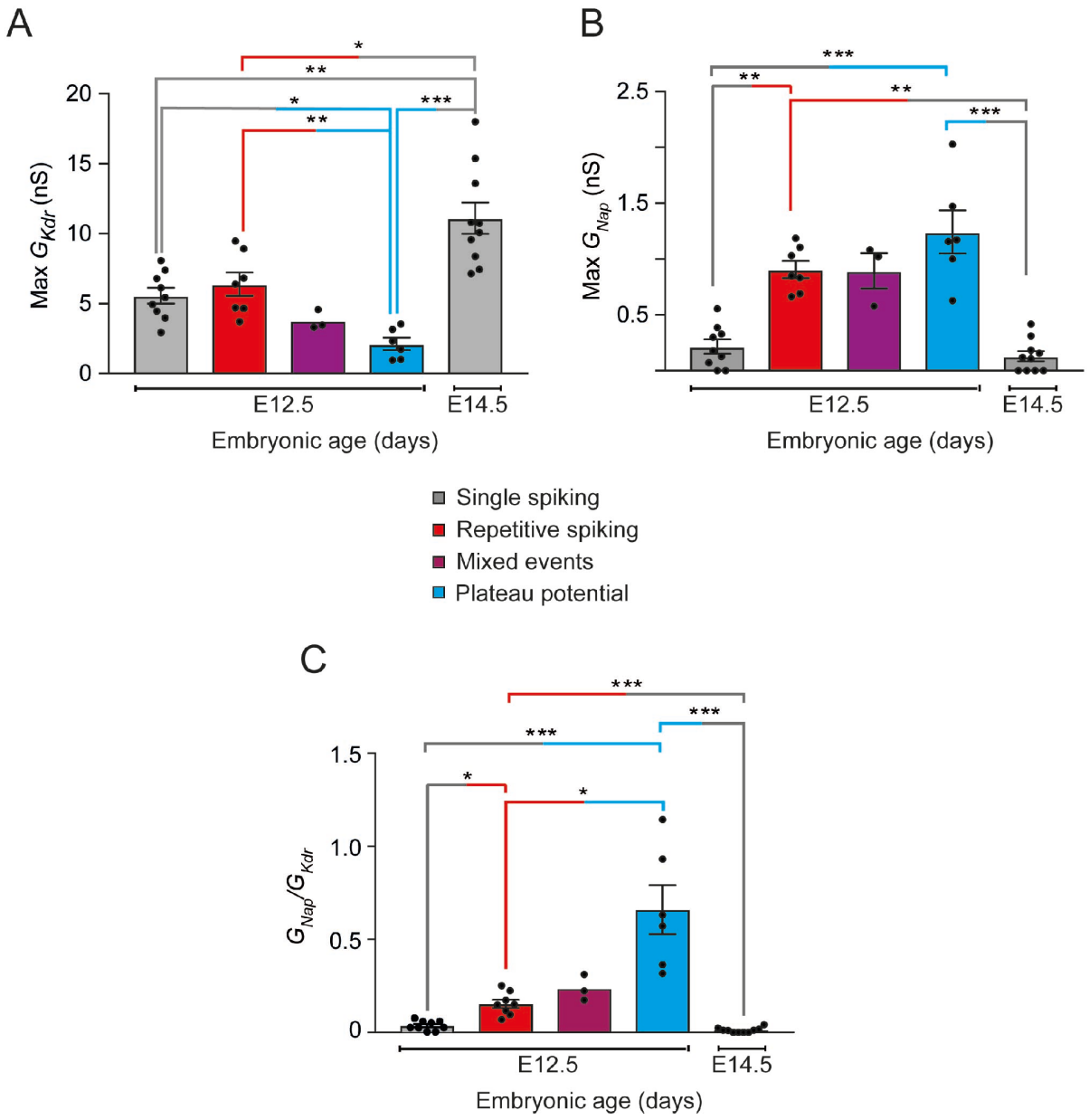

Figure 2

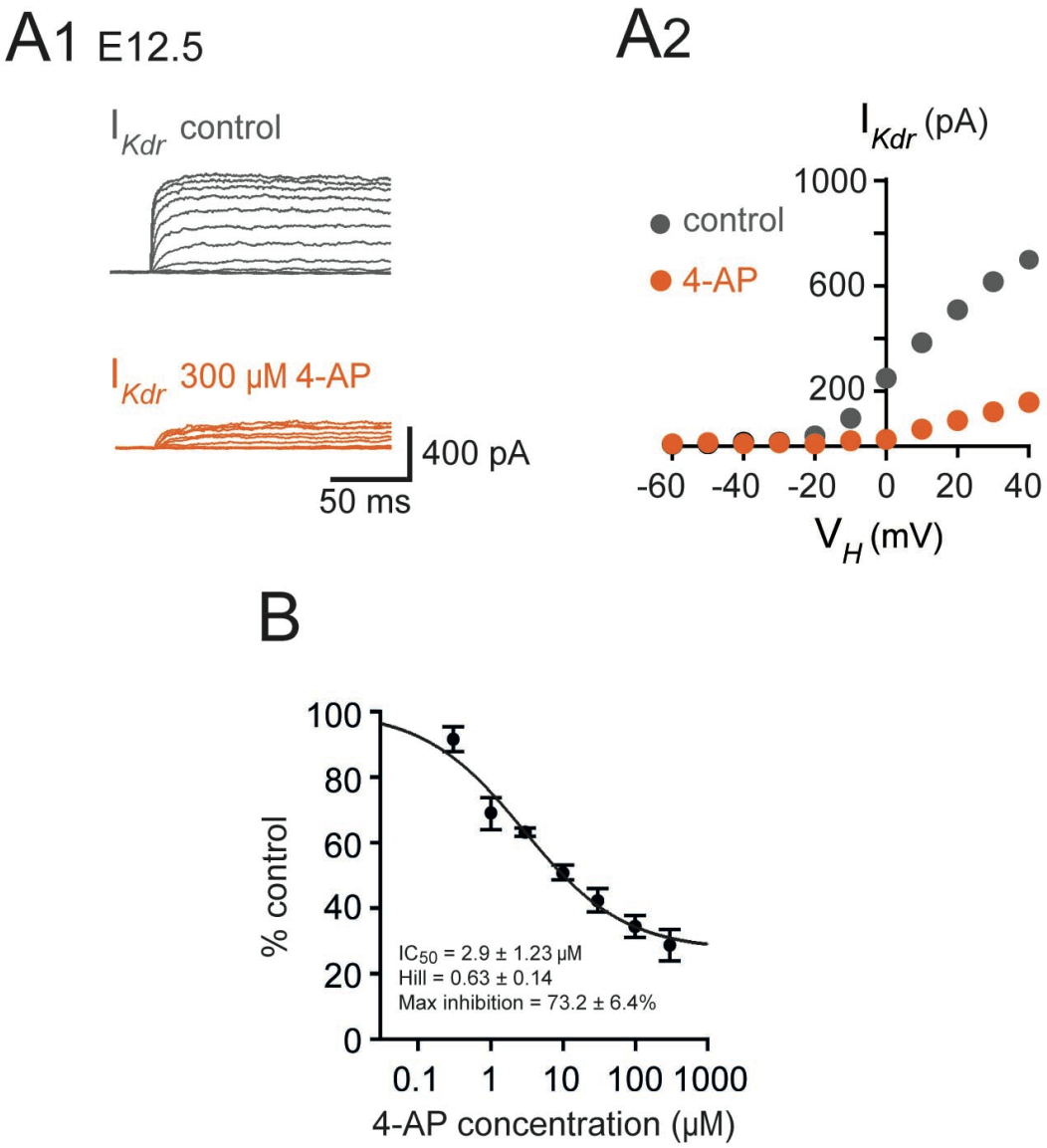

Figure 3

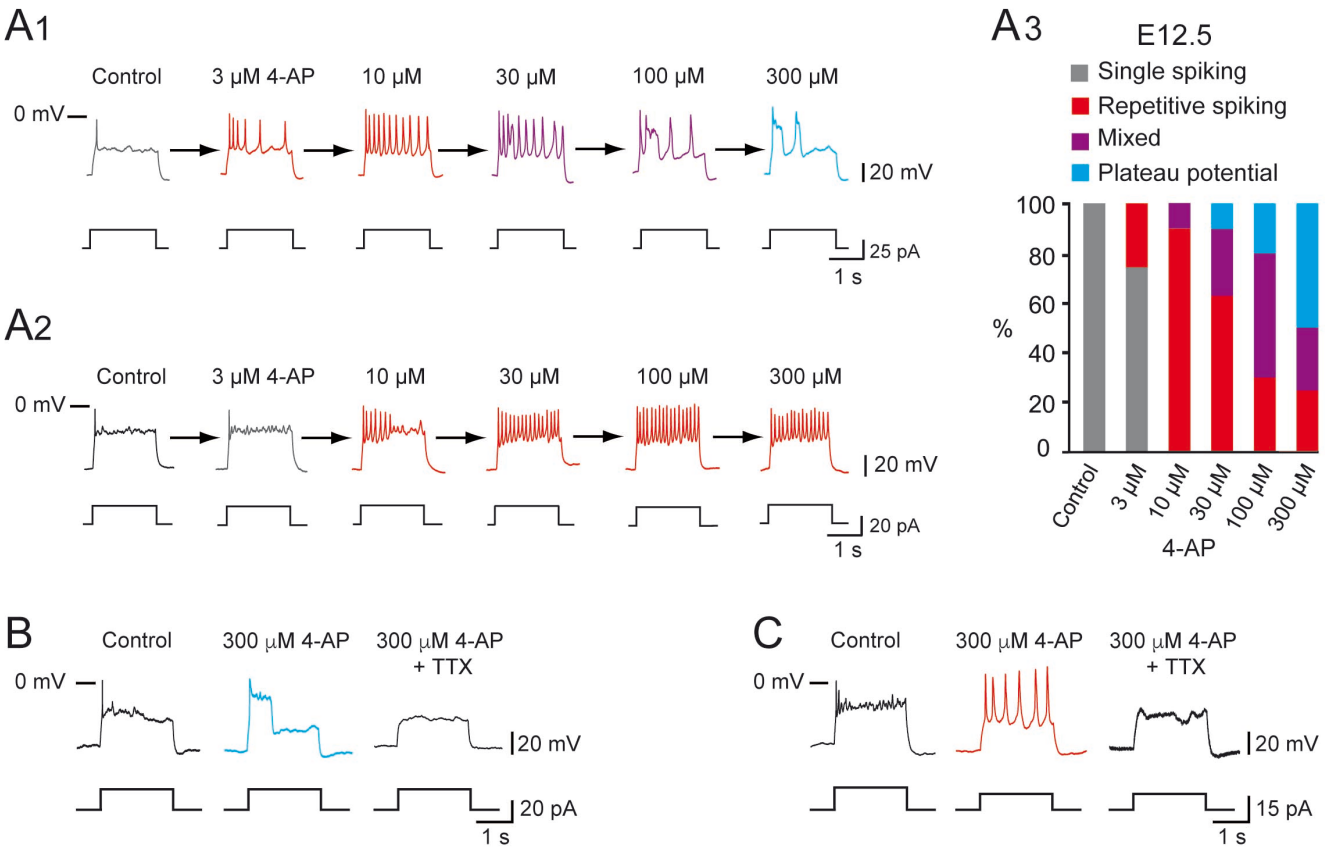

Figure 4

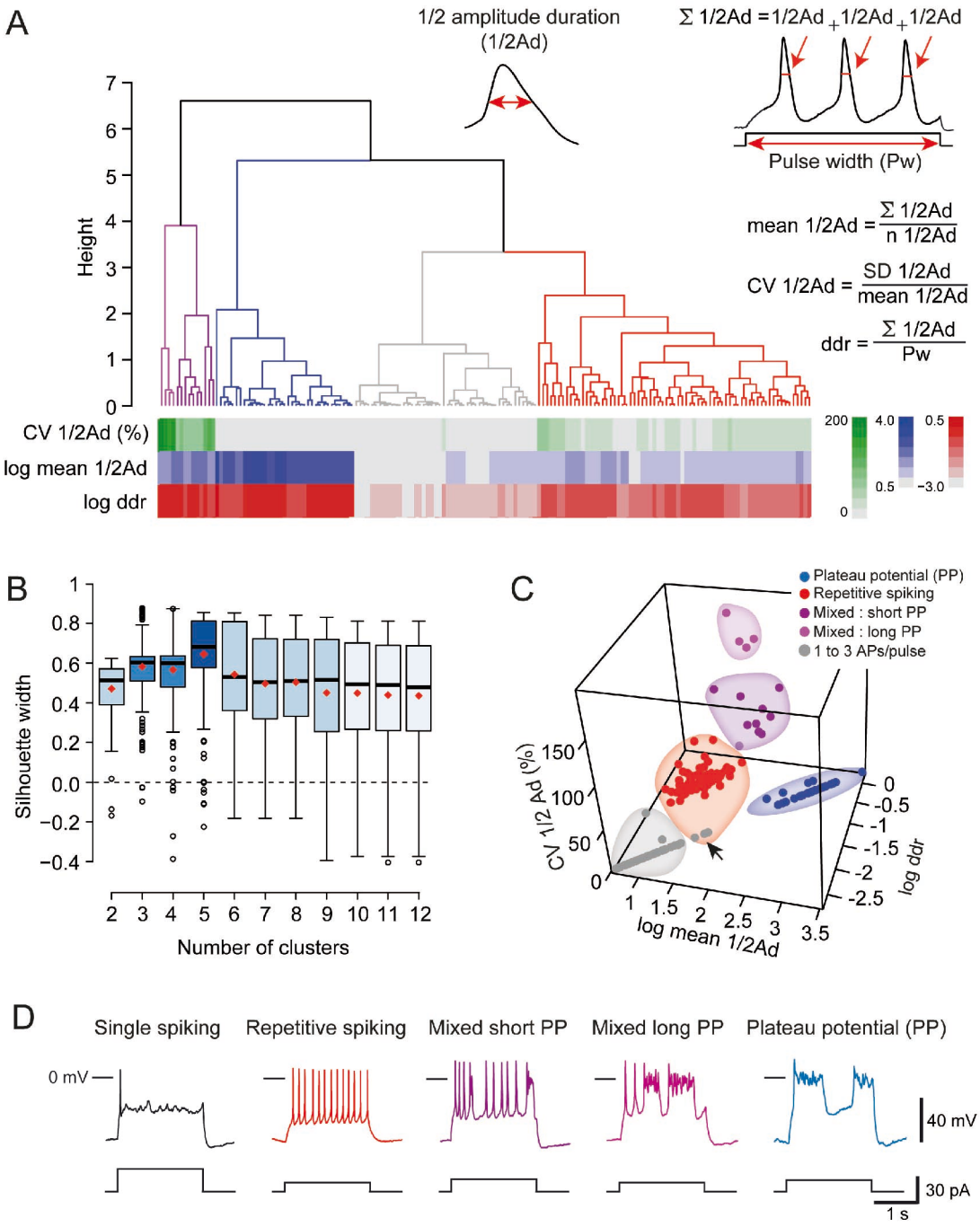

Figure 5

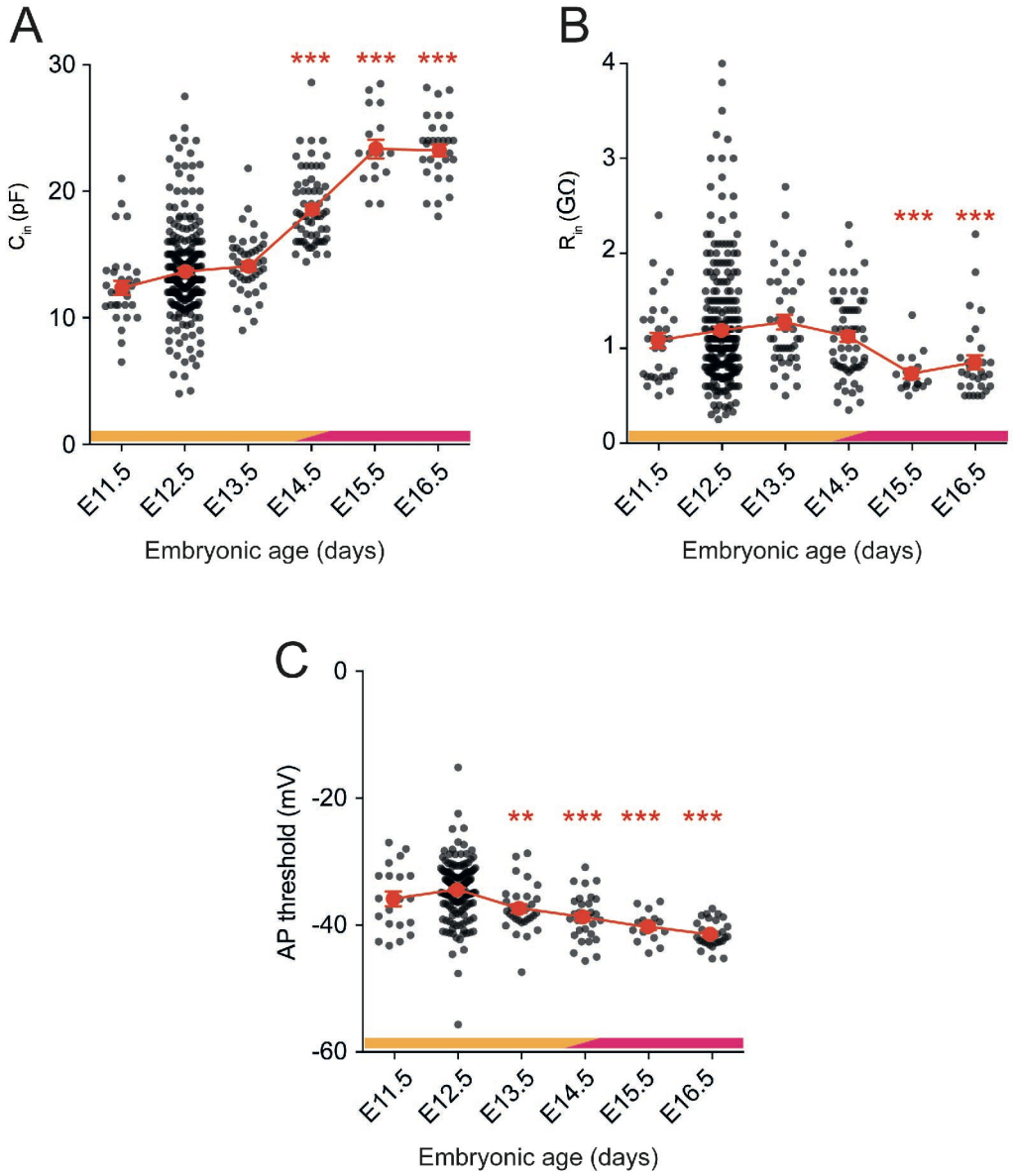

Figure 6

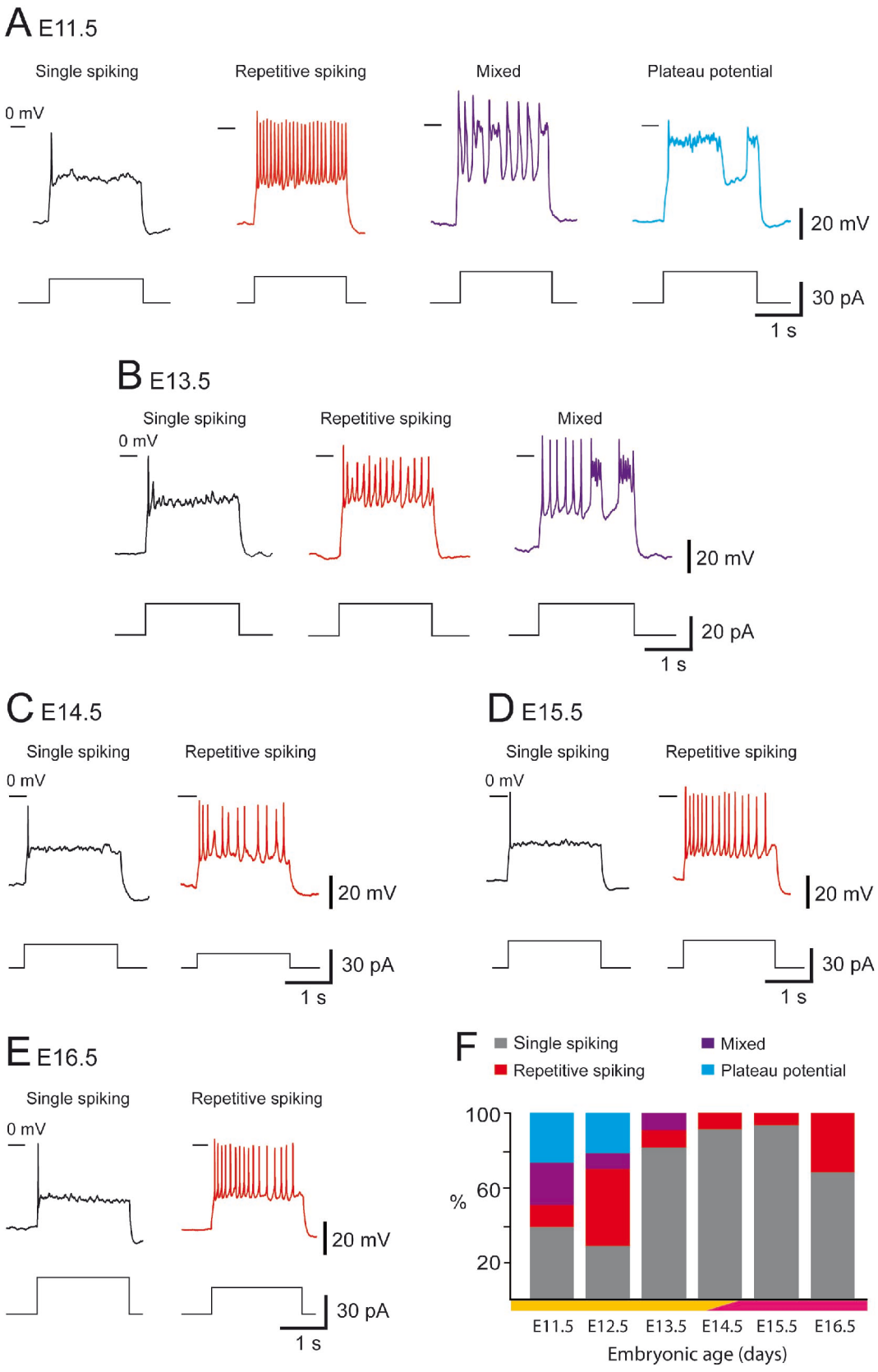

Figure 7

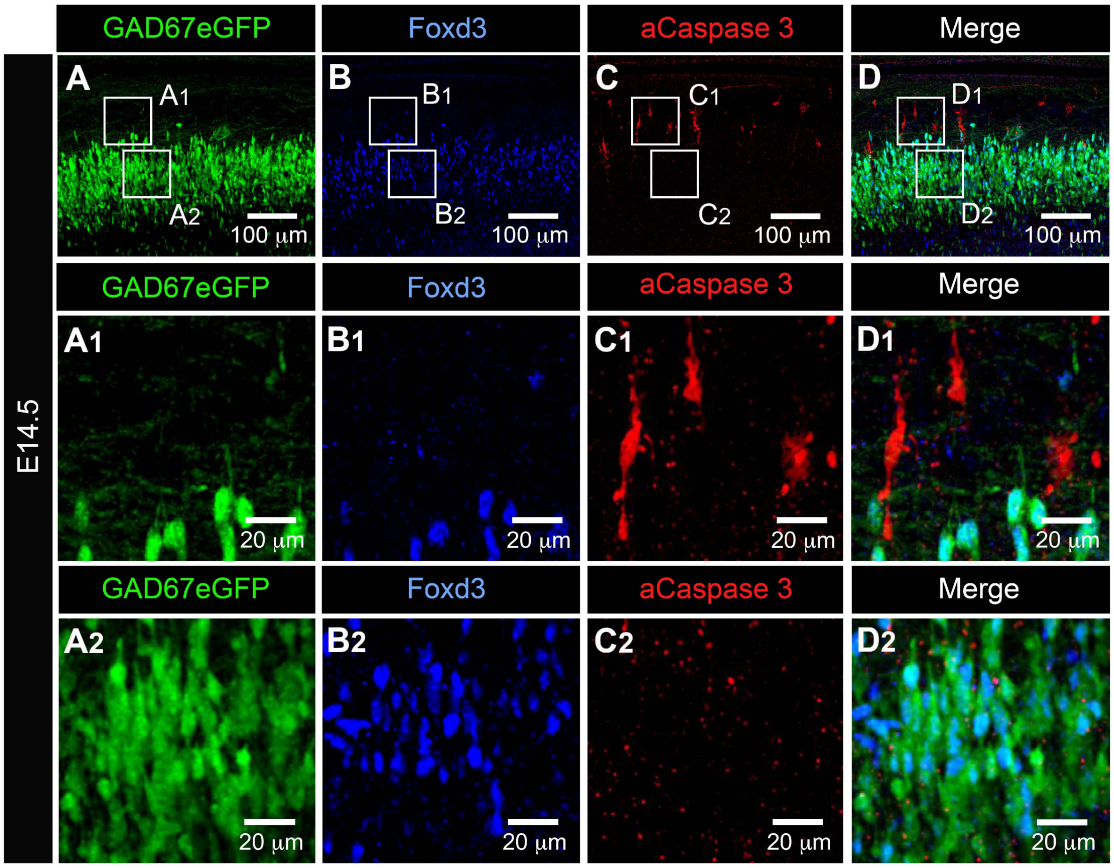

Figure 8

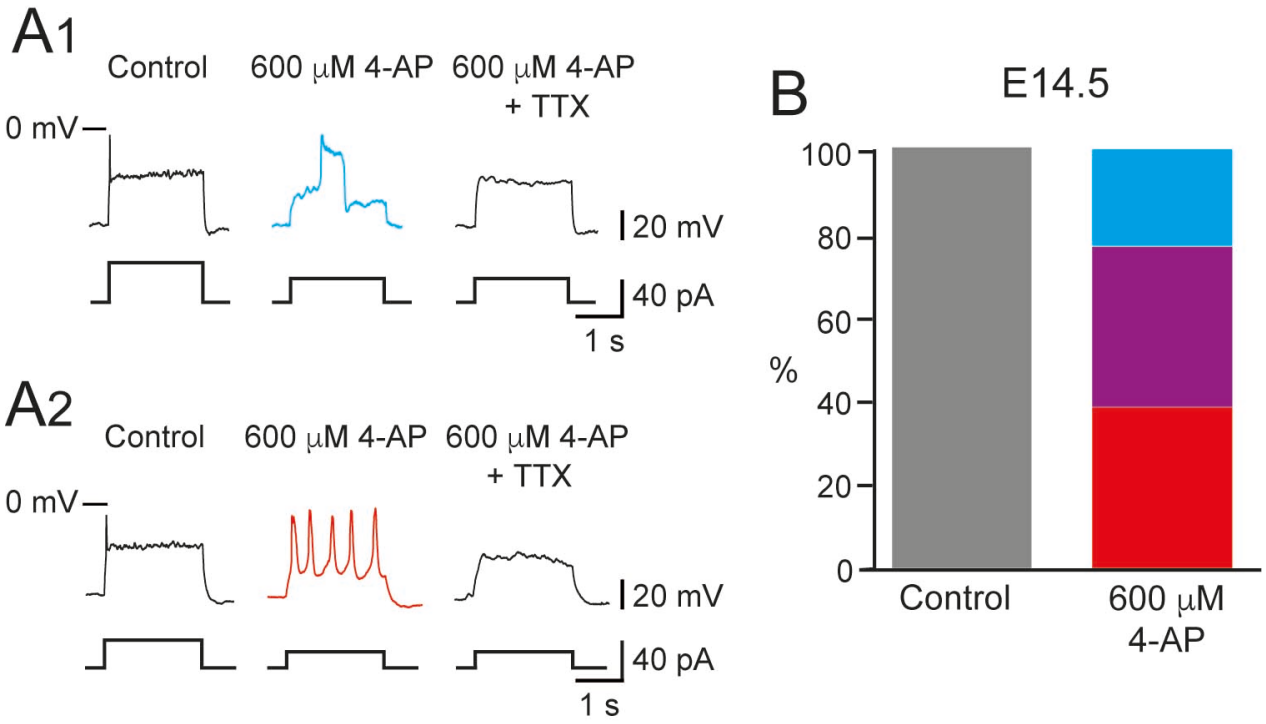

Figure 9

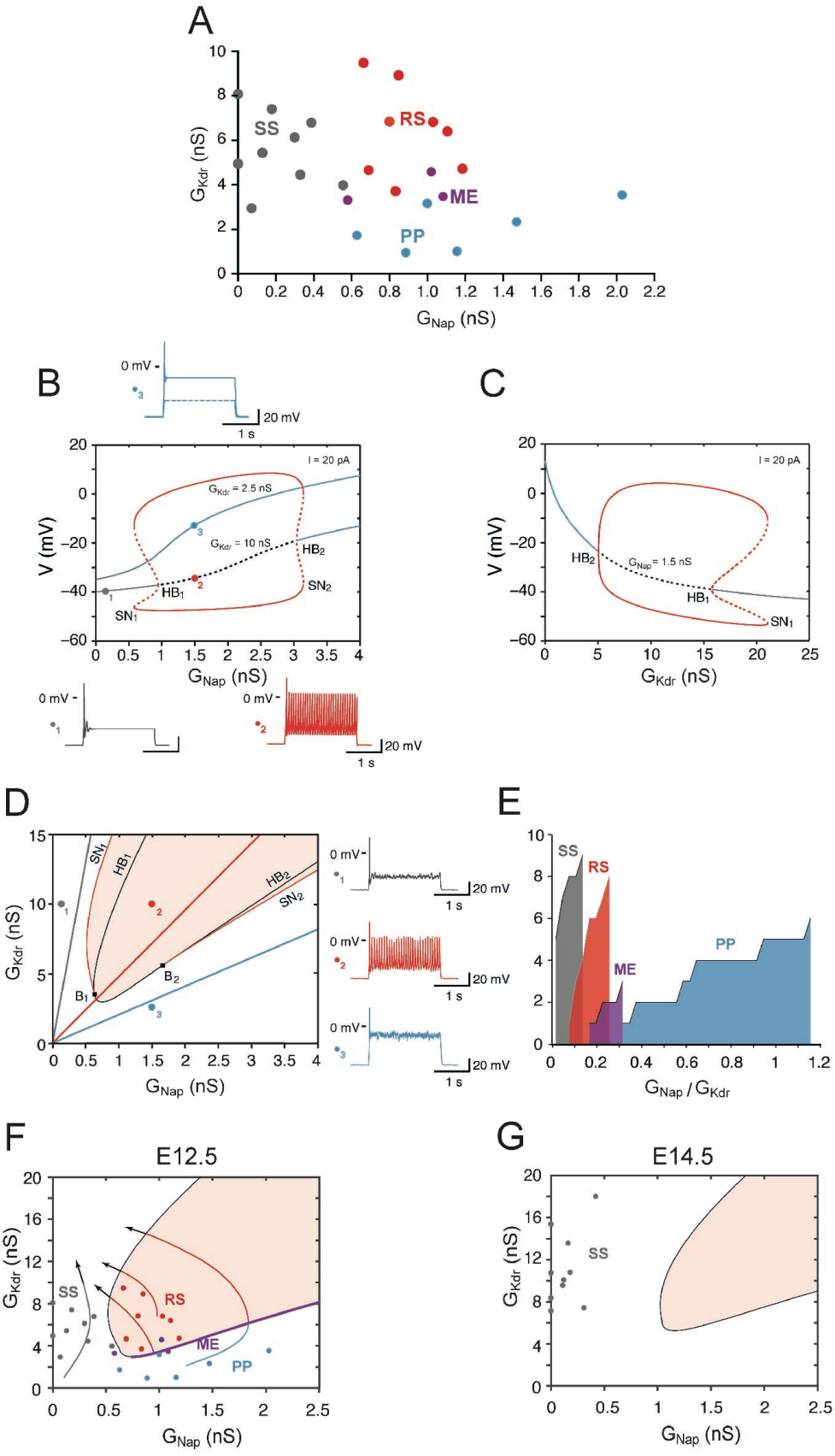

Figure 10

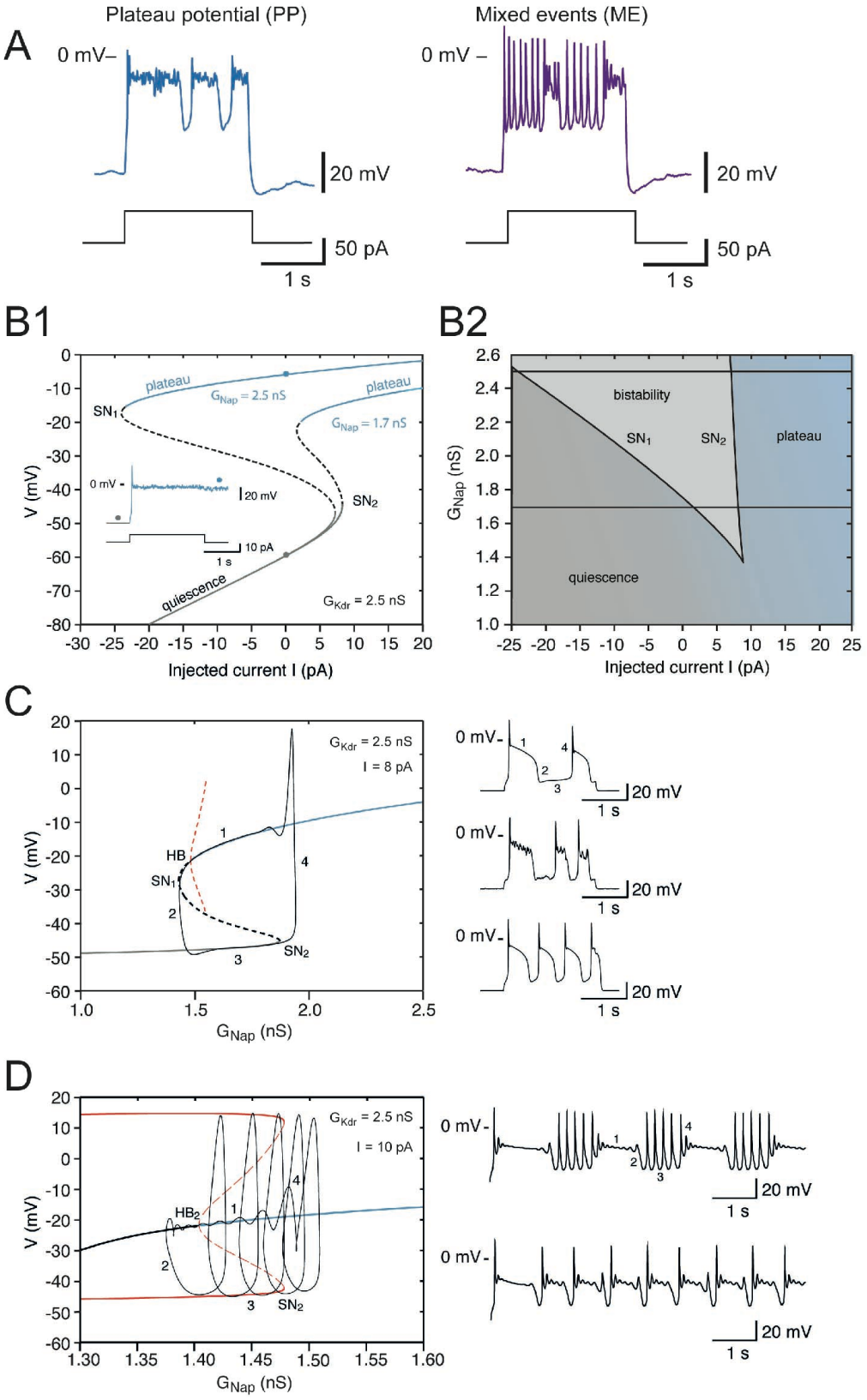

Figure 11

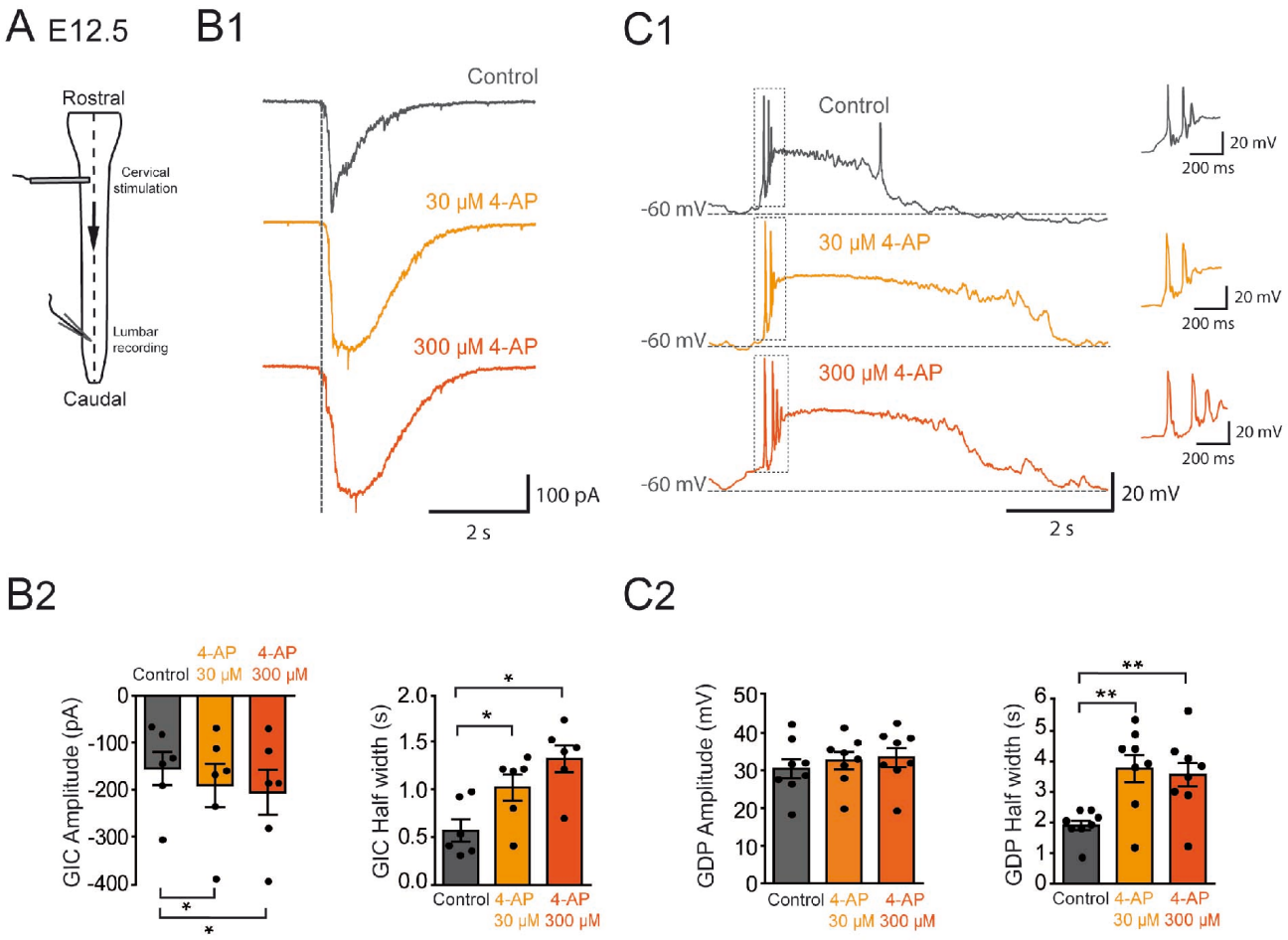

Figure 12

SUPPLEMENTARY FIGURES

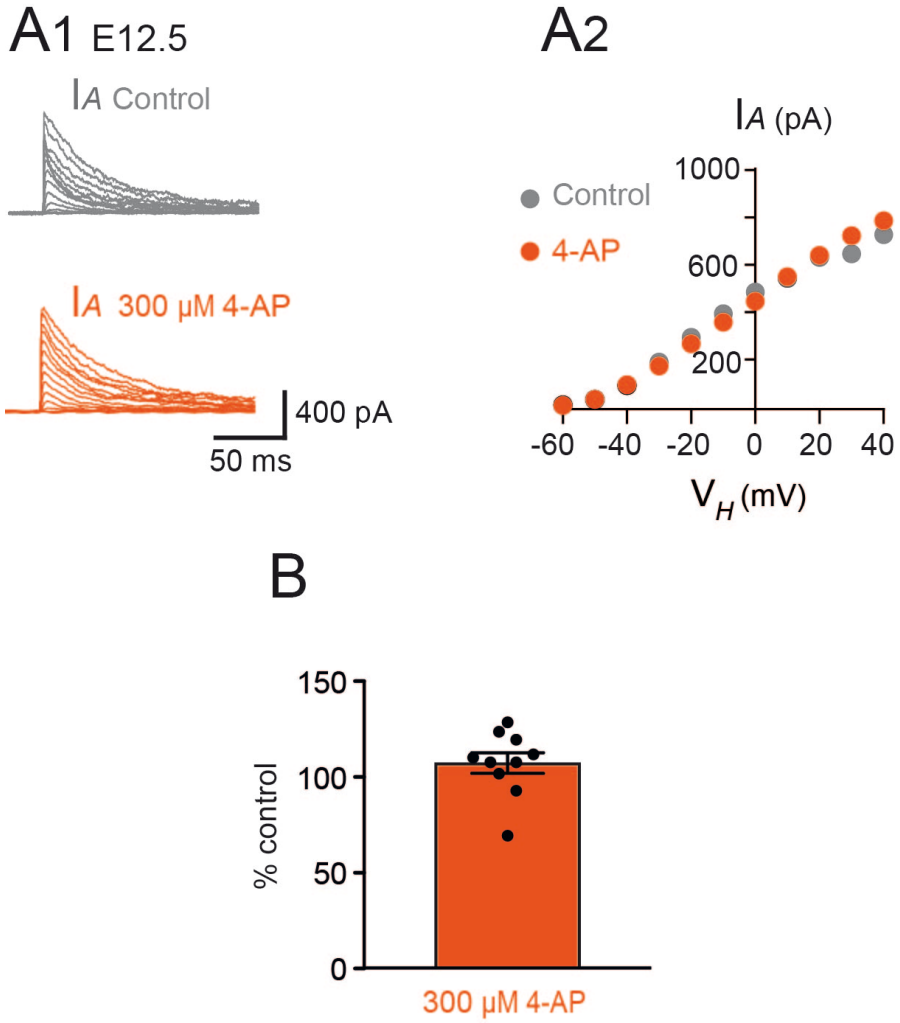

Figure 3-Figure supplement 1. I_A is insensitive to 4-AP in embryonic V1^R.
I_A was obtained as the difference between currents evoked from V_H = -100 mV and currents evoked from V_H = -30 mV (10 mV voltage step). (A1) Representative example of the effect of 300 µM 4-AP on I_A in V1^R recorded at E12.5. (A2) I_A Current-voltage ($I-V$) relationship in control conditions and in the presence of 300 µM 4-AP. The $I-V$ curves were obtained from the traces shown in A1. (B) Bar graph showing the percentage of I_A block elicited by 4-AP. Note that 4-AP did not significantly block I_A (Wilcoxon test P = 0.065, n = 10).

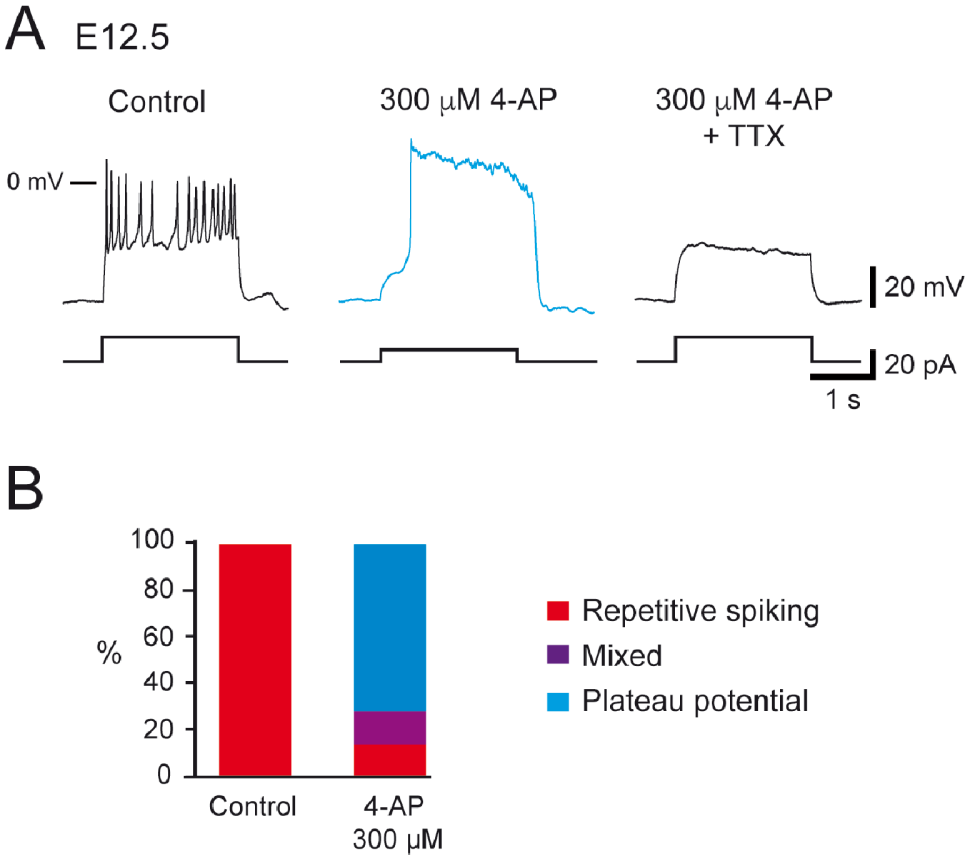

Figure 4-Figure supplement 1. Effect of 4-AP application in repetitively spiking V1^{R} at E12.5.

(A) Representative traces showing the effect of 4-AP application (300 µM) on RS V1^{R} at E12.5. Note that plateau potential activity evoked in the presence of 4-AP (middle trace) was blocked by 0.5 µM TTX (right trace). (B) Bar plots showing the changes in the firing pattern of RS V1^{R} evoked by 300 µM 4-AP application (n = 14). 4-AP application evoked a plateau potential in 71.4 % of the recorded neurons (10/14) and mixed events in 14.3% of the recorded neurons (2/14). The excitability pattern was not modified in 2 neurons.

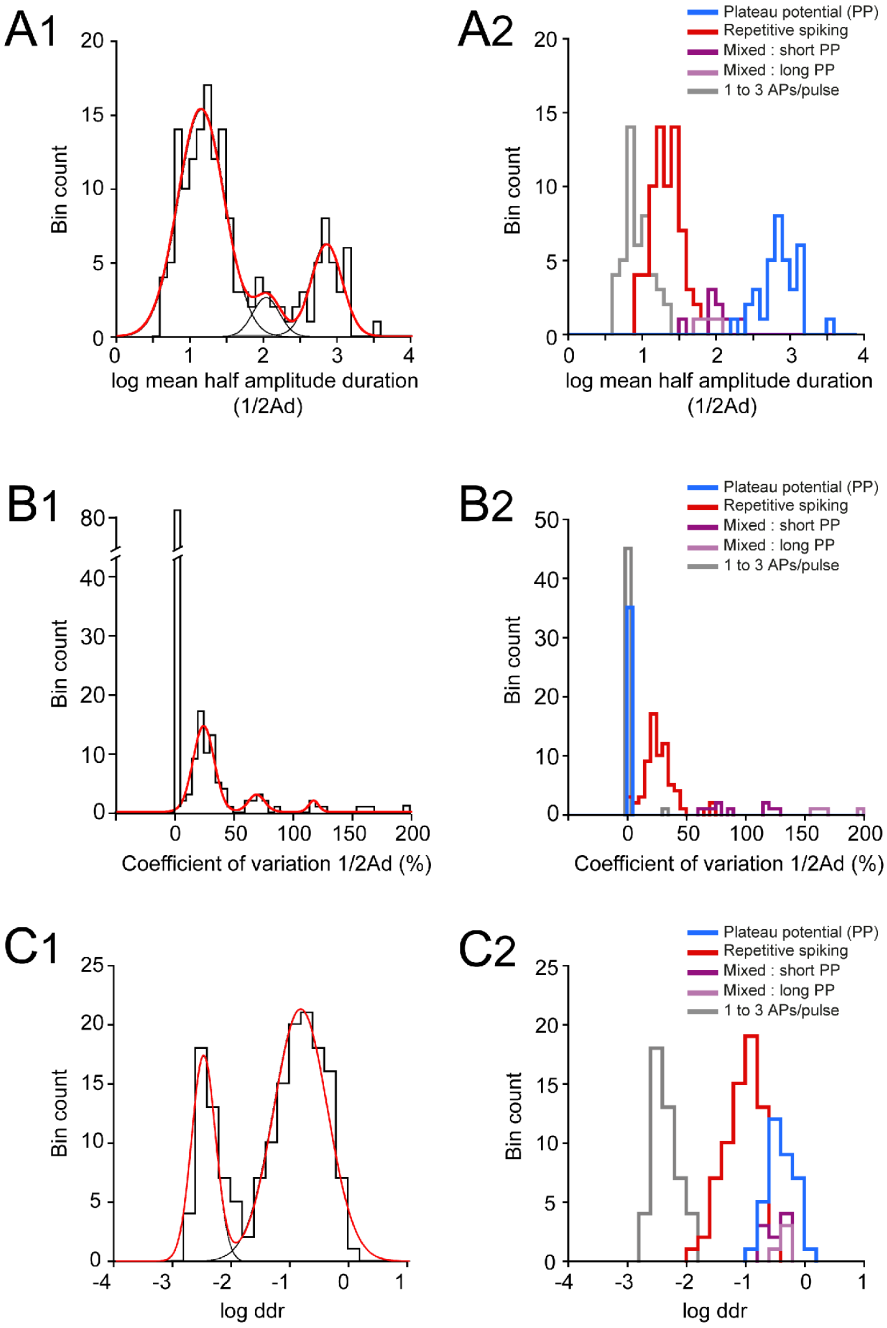

Figure 5-Figure supplement 1 : Distributions of log ½Ad, CV ½Ad and log ddr values related to the cluster analysis of embryonic V1^R firing patterns.

(A1) Histogram of log mean ½Ad (mean half amplitude event duration) for the whole V1^R population at E12.5 (n= 164; bin width 0.1). The histogram was well fitted by the sum of three Gaussian curves with means and SDs of 1.135, 2.046 & 2.84, and 0.316, 0.181 & 0.21, respectively. (A2) Histogram of the values of log mean ½Ad sorted after cluster analysis showing SS V1^R (black), RS V1^R (red), ME V1^R with short plateau potentials (ME$_s$ V1^R, light purple), ME V1^R with long plateau potentials (ME$_l$ V1^R, dark purple) and PP V1^R (blue). log

mean ½Ad was significantly different between SS $V1^R$, PP $V1^R$, the whole ME $V1^R$ population (ME_s and ME_l $V1^R$) and PP $V1^R$ (Kruskall-Wallis test $P < 0.0001$; SS $V1^R$ versus RS $V1^R$, $P < 0.0001$; SS $V1^R$ versus ME $V1^R$, $P < 0.0001$; SS $V1^R$ versus PP $V1^R$, $P < 0.0001$; RS $V1^R$ versus ME $V1^R$, $P = 0.0004$; RS $V1^R$ versus PP $V1^R$, $P < 0.0001$; ME $V1^R$ versus PP $V1^R$, $P = 0.018$; SS $V1^R$ n = 46, RS $V1^R$ n = 69, ME_s $V1^R$ n = 9, ME_l $V1^R$ n = 4, PP $V1^R$ n = 35). (B1) Histogram of CV ½Ad for the whole $V1^R$ population at E12.5 (n= 164; bin width 5%). Note that a large population of $V1^R$ had zero CV ½Ad (n = 83). The histogram for CV ½Ad ≠ 0 was fitted by the sum of three Gaussian curves with means and SDs of 23.4, 68.4 & 117 (%) and 8.9, 6.8 & 4.1, respectively. (B2) Histograms of the values of CV ½Ad sorted after cluster analysis showing SS $V1^R$ (black), RS $V1^R$ (red), ME_s $V1^R$ (light purple), ME_l $V1^R$ (dark purple) and PP $V1^R$. CV ½Ad was not significantly different between SS $V1^R$ and PP $V1^R$ (CV ½Ad of SS $V1^R$ and PP $V1^R$ = 0.682 % and 0% respectively: only one of the 46 SS $V1^R$ displayed 3 PA and had a CV ½Ad of 31.37). CV ½Ad was significantly different between RS $V1^R$ and the whole ME $V1^R$ population and also between SS $V1^R$ or PP $V1^R$ and RS $V1^R$ or ME $V1^R$ (Kruskall-Wallis test $P < 0.0001$; SS $V1^R$ versus RS $V1^R$ $P < 0.0001$, SS $V1^R$ versus ME $V1^R$ $P < 0.0001$, SS $V1^R$ versus PP $V1^R$ $P = 0.846$, RS $V1^R$ versus ME $V1^R$ $P = 0.0003$, RS $V1^R$ versus PP $V1^R$ $P < 0.0001$, ME $V1^R$ versus PP $V1^R$ $P < 0.0001$). (C1) Histogram of log ddr (sum of ½Ad divided by pulse duration) for the whole $V1^R$ population at E12.5 (n= 164; bin width 0.2). The histogram was fitted by the sum of two Gaussian curves with means and SDs of -2.51 & -0.851, and 0.2 & 0.46, respectively. (C2) Histograms of the values of log ddr sorted after cluster analysis showing SS $V1^R$ (black), RS $V1^R$ (red), ME_s $V1^R$ (light purple), ME_l $V1^R$ (dark purple) and PP $V1^R$. log (ddr) was not significantly different between ME $V1^R$ and PP $V1^R$, while it was significantly different between SS $V1^R$ and RS $V1^R$, SS $V1^R$ and the whole ME $V1^R$ population, SS $V1^R$ and PP $V1^R$, RS $V1^R$ and the whole ME $V1^R$ population, RS $V1^R$ and PP $V1^R$ (Kruskall-Wallis test $P < 0.0001$; SS $V1^R$ versus RS $V1^R$, $P < 0.0001$; SS $V1^R$ versus ME $V1^R$, $P < 0.0001$; SS $V1^R$ versus PP $V1^R$, $P < 0.0001$; RS $V1^R$ versus ME $V1^R$, $P < 0.0001$; RS $V1^R$ versus PP $V1^R$, $P < 0.0001$; ME $V1^R$ versus PP $V1^R$, $P = 0.977$). ME_s $V1^R$ and ME_l $V1^R$ differed only by their CV ½Ad (Mann-Whitney test, log mean ½Ad for ME_s $V1^R$ versus log mean ½Ad for ME_l $V1^R$, $P = 0.26$; CV ½Ad for ME_s $V1^R$ versus CV ½Ad ME_l $V1^R$, $P = 0.0028$ and log ddr for ME_s $V1^R$ versus log ddr for ME_l $V1^R$, $P = 0.1483$). It is noteworthy that the distribution of the values of each metric was multimodal thus indicating that each of them could partially discriminate different groups of embryonic $V1^R$ according to their firing pattern.

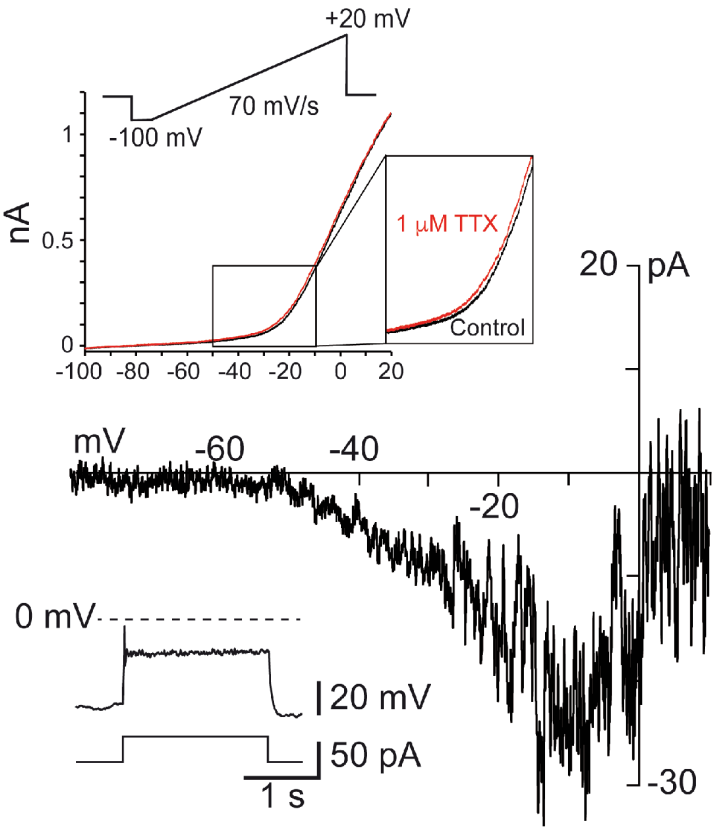

Figure 9-Figure supplement 1. I_{Nap} is present in embryonic V1^{R} recorded at E14.5. Representative trace of I_{Nap} evoked by a slow depolarizing voltage ramp (70 mV/s, upper insert) in SS embryonic V1^{R} (lower insert). I_{Nap} was isolated by subtracting currents evoked by depolarizing ramps in the presence of 1 μM TTX to the control current evoked in the absence of TTX (upper insert).

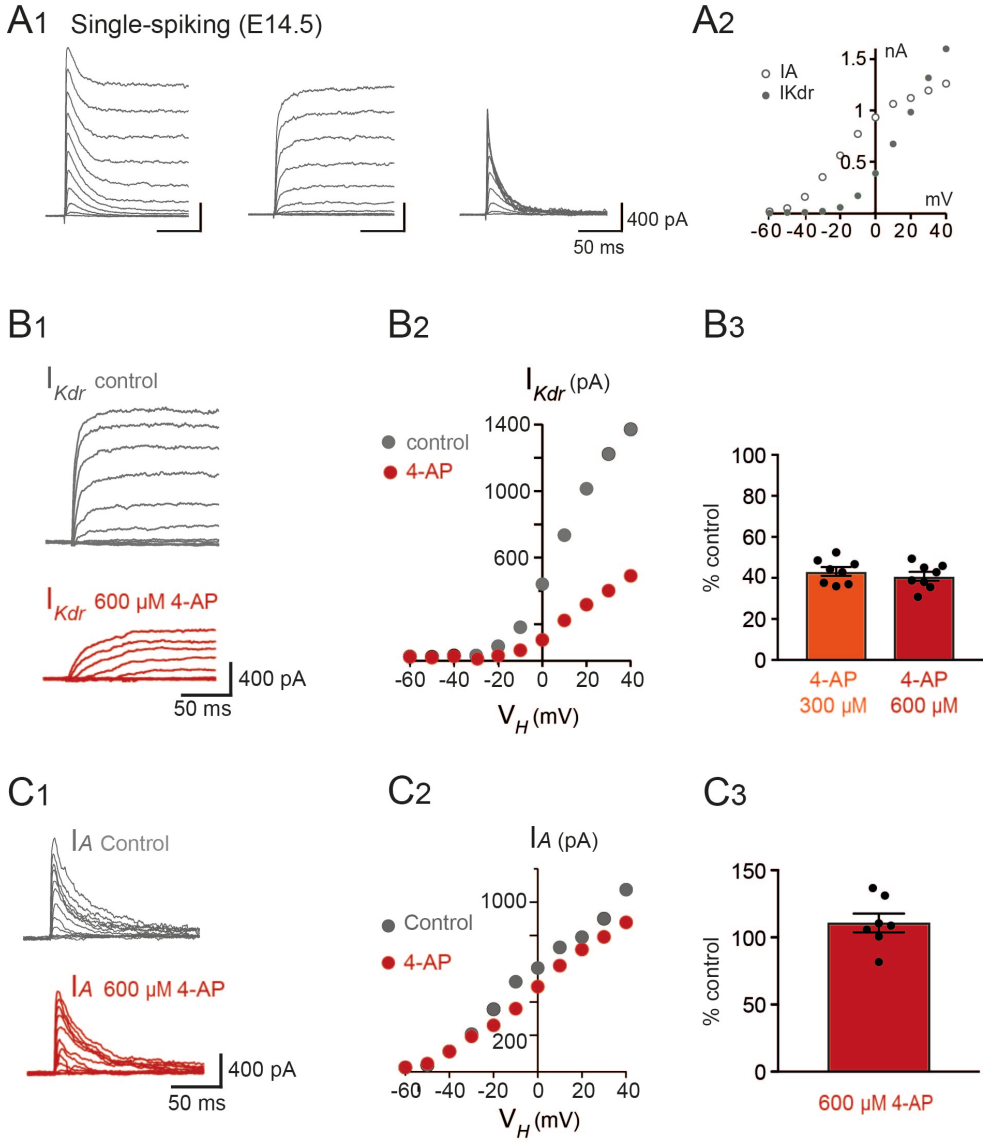

Figure 9-Figure supplement 2. I_{Kdr} was inhibited by 4-AP in V1^{R} recorded at E14.5. (A1) Representative examples of the total outward K^+ currents obtained from V_H = -100 mV (left traces), of I_{Kdr} (V_H = -30 mV, middle traces) and of isolated I_A (left traces) recorded in SS V1^{R} at E14.5. (A2) Current-voltage relationship of I_{Kdr} (filled circle) and of I_A (open circle) in SS V1^{R} at E14.5. $I-V$ curves were obtained from currents shown in A1. (B1) Representative example of the effect of 4-AP at 600 µM in V1^{R} at E14.5. (B2) Current-voltage curves in control condition and in the presence of 600 µM 4-AP. (B3) Bar plots showing the percentage of I_{Kdr} inhibition evoked by 300 µM 4-AP application (n = 8) and by 600 µM 4-AP application (n = 7). The percentages of I_{Kdr} inhibition evoked by 300 µM 4-AP and by 600 µM 4-AP applications were not significantly different (P = 0.574). (C1) Representative example of the effect of 600 µM 4-AP on I_A in V1^{R} recorded at E14.5. (C2) $I-V$ curves in control conditions and in the presence of 600 µM 4-AP. These curves were obtained from the traces shown in B1. (C3) Bar graph showing the percentage of I_A block elicited by 4-AP. 4-AP did not significantly block I_A (Wilcoxon test P = 0.11, n = 6).

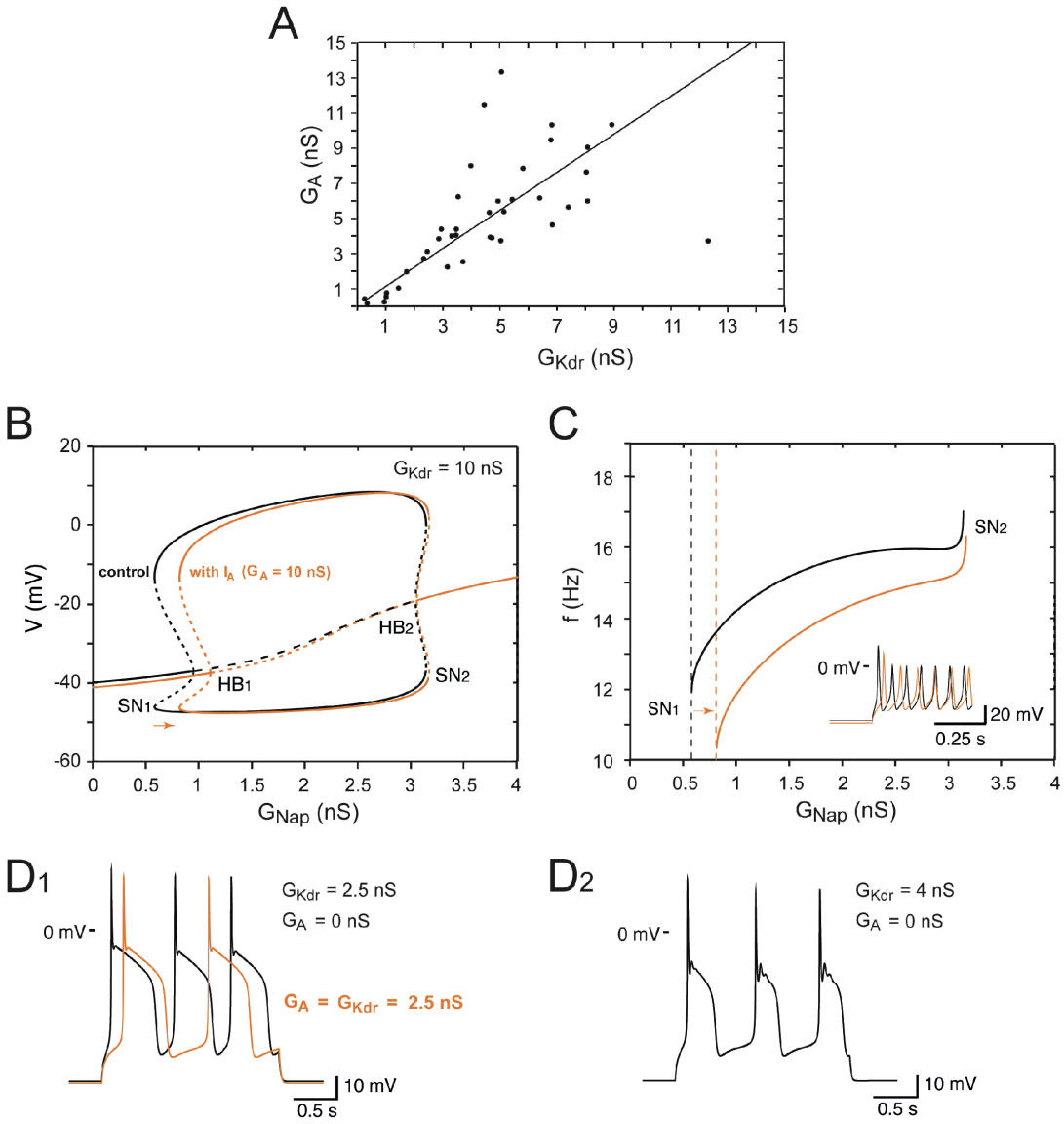

Figure 10-Figure supplement 1. Effects of I_A on embryonic V1^R firing patterns predicted by computational modeling.

(A) The maximal conductances of I_{Kdr} and I_A at E12.5 are linearly correlated. Best fit: G_A = 1.09 G_{Kdr} (R^2 = 0.81, N=44). (B) Effect of I_A on the dynamics of the basic model. The one-parameter bifurcation diagrams in control condition (black, G_{Kdr} = 10 nS, no I_A, same as in Fig 9B) and with I_A added (orange, G_A = 10 nS) are superimposed. The I_A current shifts the firing threshold SN_1 to the right by 0.234 nS (from G_{Nap} = 0.582 nS to G_{Nap} = 0.816 nS, see also C) as indicated by the orange arrow, without affecting the amplitude of action potentials (see also insert in C). In contrast, I_A shifts SN_2 by only 0.025 nS because it is inactivated by depolarization. (C) I_A also slows down the discharge frequency, as shown by comparing the $G_{Nap} - V$ curves without I_A (black) and with I_A (orange). For G_{Nap} = 1 nS, for instance, the firing frequency is reduced by 16.7%, from 14.19 to 11.82 Hz. Here again, the effect of I_A progressively decreases as G_{Nap} increases because of the membrane depolarization elicited by I_{Nap}. For G_{Nap} = 3 nS, for instance, the firing frequency is reduced by 5% only, from 15.96 to 15.16 Hz. The frequency reduction elicited by I_A does not merely result from the increased firing threshold; when shifted to the right by 0.234 nS, the control $G_{Nap} - V$ curve still does not overlap with the $G_{Nap} - V$ curve obtained for G_A = 10 nS (not shown). Note that

the latency of the first spike is increased (see voltage trace in insert), which is a classical effect of I_A. (D) In the pseudo-plateau bursting regime, the I_A (G_A = 10 nS) lengthens the repolarizing phase without affecting the duration of plateaus much, as shown by the comparison of the voltage traces obtained without I_A (control, black) and with I_A (orange) in D1. This is because I_A is activated near rest but inactivated during voltage plateaus. In the example shown, only two plateaus occur during the 2 s current pulse, instead of three in the control condition. Note also that the latency of the first plateau is increased. Increasing G_{Kdr} to 4 nS, in the absence of I_A, similarly lengthens repolarization episodes, as shown in D2. However, plateaus are shortened and display some spikelets, at variance with D1. This is because I_{Kdr} does not inactivate (or does it only very slowly), in contrast to I_A.

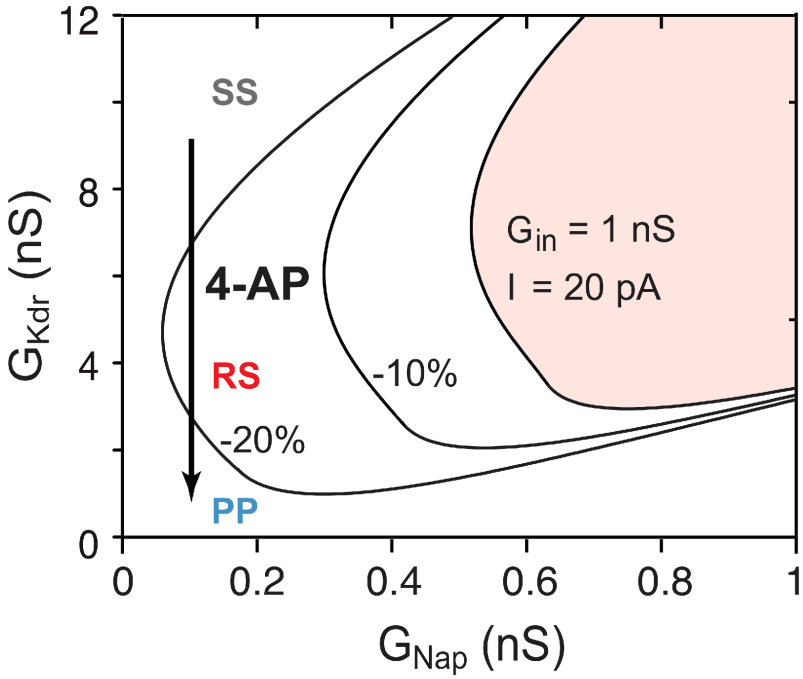

Figure 10-Figure supplement 2. Influence of input conductance changes on the bifurcation diagram.

The RS region of the basic model is displayed in the $G_{Nap} - G_{Kdr}$ plane in control condition for E12.5 V1^{R} (C_{in} = 13 pF, G_{in} = 1 nS, I = 20 pA, shaded area), and when G_{in} and I were both reduced by 10% (middle curve) or by 20% (left curve). The reduced I accounts for the decrease in rheobase following the decrease in G_{in}. If 4-AP reduced only G_{Kdr} (as indicated by a downward arrow) the firing pattern of SS V1^{R} would not change, the control RS region being too far to the right to be visited. In contrast, when the effects of 4-AP on the input resistance and rheobase are taken into account, the bifurcation diagram moves closer to the origin of the $G_{Nap} - G_{Kdr}$ plane, and the RS and PP regions are then successively entered as G_{Kdr} is reduced. The same explanation holds at E14.5.